HIGH EXTINCTION RATIO MID-INFRARED POLARIZER BASED ON SULFURIC POLYMER

A Thesis

Submitted to the Faculty

of

Purdue University

by

Aaron James Berndt

In Partial Fulfillment of the

Requirements for the Degree

of

Master of Science in Mechanical Engineering

August 2018

Purdue University

Indianapolis, Indiana

THE PURDUE UNIVERSITY GRADUATE SCHOOL
STATEMENT OF COMMITTEE APPROVAL

Dr. Jong E. Ryu, Chair

Department of Mechanical and Energy Engineering

Dr. Andres Tovar

Department of Mechanical and Energy Engineering

Dr. Vemuri Gautam

Department of Physics

Dr. Rui Cheng

Department of Physics

Approved by:

Dr. Sohel Anwar

Chair of the Graduate Program

To my family and friends.

ACKNOWLEDGMENTS

I would like to first thank my advisor, Dr. Jong Eun Ryu, for his guidance and encouragement he has provided to me over the course of my research. He has helped me realize my own potential and perform at a higher level than I thought possible. Next, I would like to thank the other members of the committee, Dr. Gautam Vermuri, Dr. Ruihua Cheng, and Dr. Andres Tovar, for taking an interest in my research and investing the time to review and improve my work.

I would also like to acknowledge the support I received from the Air Force Research Lab staff and facilities over the course of my research with special thanks to Dr. Augustine Urbas and Dr. Zahyun Ku. I would like to thank Dr. Urbas for his help in shaping the direction of this project and his guidance along the way. I would also like to thank Dr. Ku for his insight on the testing and simulation performed during this project.

I would also like to acknowledge the support I received from Argonne National Lab staff and facilities with a special thanks to Dr. David Czaplewski for his invaluable help with the design and fabrication of the sample molds used for my work.

I would like to thank my fellow research group members who have been great resources and even better friends. One could not hope for better lab mates.

Finally, I would like to thank my family and friends; without their support I would not have been able to finish this work. Special thanks to my parents who have always encouraged me to pursue an education and realize my goals.

TABLE OF CONTENTS

LIST OF TABLES

LIST OF FIGURES

Figure Page

Figure Page

ABSTRACT

Berndt, Aaron James. M.S.M.E., Purdue University, August 2018. High Extinction Ratio Mid-Infrared Polarizer Based on Sulfuric Polymer. Major Professor: Jong E. Ryu.

Transparent polymers with low-loss and high refractive index are critical components of integrated optical devices including filters, lenses, and polarizers. Current conventional mid infrared (MIR) polarizers are fabricated from inorganic semiconductor materials and are intrinsically expensive, brittle, and difficult to manufacture. This represents a significant challenge in developing a surface mountable low-cost component. Herein, an alternative sulfur polymer-based material will be used to create MIR polarizers reducing cost and simplifying fabrication. Sulfur polymer ellipsometry data indicates low loss material with a refractive index of 1.64 across the MIR spectrum. Transmission data of thin film samples also support the fact that sulfur polymer is transparent in the MIR with an even transmission through the range. Sulfur polymer was created by the mixing of molten sulfur with 1-3, diisopropenylbenzene (DIB) and allowing the chains of sulfur rings to break open and cross link with the DIB. To form the polarizer, sulfur polymer solution was spin-coated onto a silicon (Si) wafer and imprinted with a polydimethylsiloxane (PDMS) linear grid stamp. After imprinting, a thin layer of gold was deposited onto the surface of the grating, completing the bilayer structure polarizer.

To measure the performance of the polarizer, transverse magnetic (TM) and transverse electric (TE) transmission data was collected with an Fourier-transform infrared spectroscope (FTIR). The linear polarizer should allow transmission of the TM light while blocking all TE light. The extinction ratio (dimensionless) is used to compare the two polarization states, defined as the TM transmission divided by the TE transmission.

With high refractive index and transmission in MIR sulfur polymer is ideal for fabrication of optical components and can be applied as a substitute for conventional brittle inorganic materials. Sulfur polymer based polarizers showed experimental FTIR TM transmission over 95 percent. Combined with low FTIR TE transmission the physical samples displayed extinction ratios of over 600 in MIR. High polarization performance is attributed to the surface plasmon effect along the grating surface as well as the Fabry–Pérot cavity conditions between the multiple films. These assumptions are reinforced by the correlation between the simulation data and experimental results.

1. INTRODUCTION

1.1 Mid Wavelength Infrared Sensors

MIR detection can give very unique spectral data that would otherwise not be apparent with conventional visible light detection. Many guidance systems and satellites utilize MIR detection to gather information about the movement of objects, but these systems are not ideal and have limitations. With the addition of polarimetric data, these MIR systems will increase their capabilities and add an additional layer of information for the end user. Mid wavelength infrared (MIR, 3-5 μm) detectors and sensors are widely used for a variety of applications, including non-invasive medical diagnostics, industrial and military applications such as gas detection, night vision, overhead intelligence systems, and thermal track and search [1].

Many of these optical systems rely on MIR polarizers integrated into the imaging system to provide contrast or enhance image contrast by remove incidental light . Current polarizer technology relies on labor intensive manufacturing and results in excessive cost. Herein, is discussed an alternative sulfur polymer-based material which has been used to create MIR polarizers reducing cost and simplifying fabrication.

Similar to the limitations of visible light detectors, MIR detectors have difficulty distinguishing objects hidden by shadow or inclement weather. In order to resolve the limitations of MIR detectors, visualization of light polarization provides additional information about the intensity and wavelength, including surface features, shading, and roughness [2, 3]. Not only does the polarimetric sensing enhances contrast and definition of images, it also enhances the ability to distinguish the difference between radiation of man-made and natural materials, such as camouflage [2, 4]. This enhancement in definition is shown in Fig. 1.1, below, where the two images in Fig. 1.1 (a) are both taken with a standard IR detector compared to the two images in Fig. 1.1 (b) which were captured with a polarimetric IR detector.

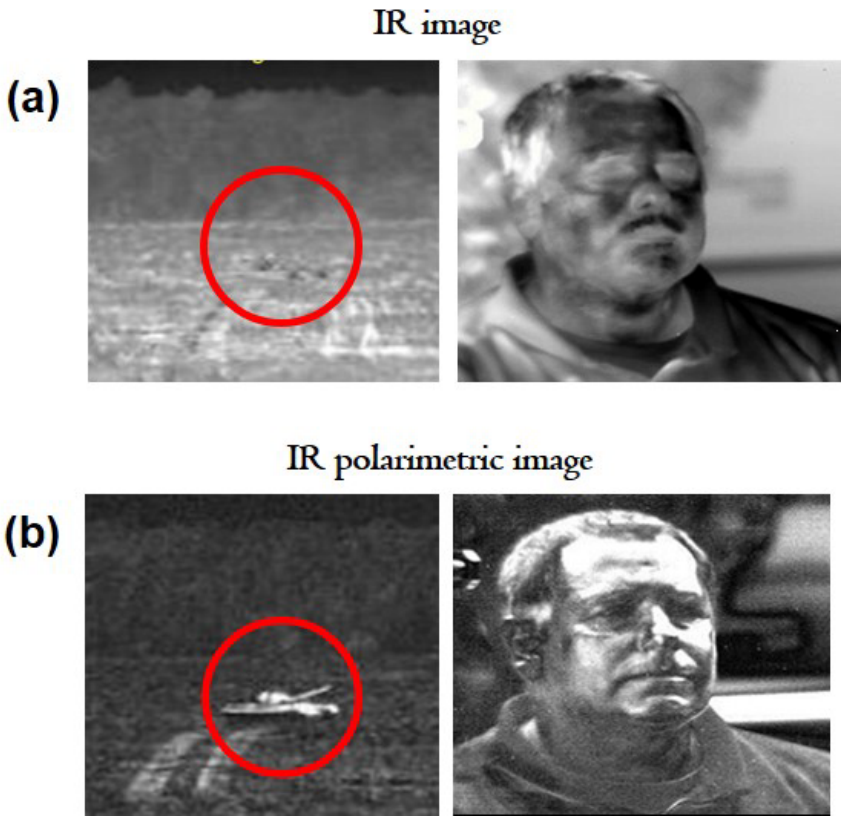

Figure 1.1. Display of polarimetric imaging: In figure (a) standard IR images are displayed. Figure (b) The same images are displayed with the additional polarimetric data [5]

1.2 Motivation of the Study

In the MIR range, most common polarizers are ruled, holographic, or etched wire grid polarizers. In order to create the very thin grid traces, ruled structures utilize a thin diamond tipped needle that physically deform the surface of the material to create the desired pattern [6]. This process takes much time and is limited by the speed and size of the needle, also the materials used in this process must be hard and non- granular like ZnSe. Holographic polarizers are formed by the interference lithography pattern of two coherent laser beams that expose a periodic pattern of photoresist which is then developed and coated with a conductive metal [7]. Etched wire grid polarizers are formed by nano imprint lithography (NIL) or interference

lithography (IL) patterning of photopolymer which is used as a sacrificial mask for reactive ion etching. Etching is performed to cut the pattern into the substrate, the photoresist is then lifted off leaving the conductive substrate with an etched periodic grating [8]. Etched polarizers are fabrication intensive and can suffer from pinhole defects, a leading cause of low extinction ratios [9]. Current conventional IR optical components are fabricated based on inorganic semiconductor materials such Ge, ZnSe, and ZnS [10]. While these inorganic materials have high index of refraction (n) and high transmission in IR regime, they are intrinsically expensive, brittle, difficult to manufacture and not suitable for integration with surface mounted components [10, 11].

As an alternative, polymer based wire grid polarizers involve a simple low cost fabrication process that can be performed on a variety of material substrates. Polymer wire grid polarizers are formed by creating a periodic wire grid structure by either NIL or IL, then a conductive metal film is deposited on the surface creating two layers of wire grids separated by the polymer height. Examples of this include NIL patterning of polymethyl methacrylate (PMMA) directly on silica followed by Au evaporation; no etching or liftoff is necessary. Experimental ellipsometry results show polarization extinction ratios of over 200 in the visible spectra [12]. IL has also been used to create PMMA patterns on quartz substrate followed by evaporation deposition of Al, also providing high extinction ratios above 200 [9]. This process is self-masking, greatly reducing the effect of pinhole defect generation by covering any irregularity in the pattern with the conductive metal film.

By utilizing the NIL polymer fabrication technique, state of the art imaging devices can be directly integrated with patterned wire grid polarizers. Polymer spun across the surface of a focal plane array (FPA), patterned into the wire grid array and deposited with conductive metal, creates a wire grid polarizer directly on the surface of the imaging device. This method reduces cost by simplifying the manufacturing to one-step of lithography that can easily be integrated into current semiconductor

fabrication. The direct surface integration allows for a compact polarimetric imaging system, reducing alignment error and limiting need for recalibration [2].

Sulfur is a significant component of sulfur polymer, consisting of 35 percent of the polymer structure by weight. Sulfur is a natural element and is in abundant supply because it is a byproduct of the petroleum refining process [13]. The production of sulfuric acid, the main component in many fertilizers, is the main industrial use of sulfur and cannot keep pace with sulfur production. Due to the limited industrial applications of sulfur an abundance of sulfur is stockpiled around the world, which allows for a unique opportunity to utilize low cost material into a functional optical polymer.

Herein, a novel polymer was fabricated and characterized, original 1-D subwavelength grating structures were designed and fabricated, wire grid polarizers were fabricated, tested, and simulated to enhance performance in MIR polarimetric imaging.

1.3 Objective

The objective of this research is to design, create and evaluate the performance of a sulfur polymer based subwavelength polarizer. An in depth characterization of the optical properties will be presented as well as a comparison of different grating design configurations. By comparing the experimental and simulated results an optimal grating design was chosen and fabricated. This research aims to further explore surface mountable polarizers by utilizing new MIR materials and designs, characterize the new polarizer performance and compare to simulation results. By establishing accurate relationships between experimental and simulation results, greater understanding of the wire grid polarization mechanism is shown.

1.4 Overview of Thesis

This work is broken into six chapters that outline the entire process of this research project. The first section outlines the motives and overall goals of this work. Including

a literary review of the current state of MIR polarizers and ending with a summary of the current issues with MIR detection and how this research can directly overcome these limitations.

The second chapter goes into the technical background of this work and explains many of the concepts featured in the research. Chapter three describes the fabrication of the polymer material used throughout, the fabrication process of the master molds as well as the sample fabrication of the polymer polarizers. Chapter four goes into details of the physical tests performed including: ellipsometry and FTIR. Each testing procedure is outlined, results are stated, and impact of results is discussed. Chapter five then discusses the simulated analysis of the polymer polarizers and compares the theoretical values with the experimental data from chapter four.

The concluding chapter is a summary of the topics described above, statement of the conclusions drawn from this research, and recommendations for future work.

2. BACKGROUND

2.1 Polarization

Polarization is a property of transverse electromagnetic waves and can be random, linear, circular or elliptical. For this thesis, when describing polarization it refers to the linear polarization state. Electromagnetic waves consist of two oscillating waves, one electric and one magnetic that both perpendicular to each other as well as perpendicular to the direction of motion, this type of wave is known as a transverse wave. Fig. 2.1 shows the change in polarization state of light from randomly oriented to linearly polarized as the transverse beam passes through the linear polarizer.

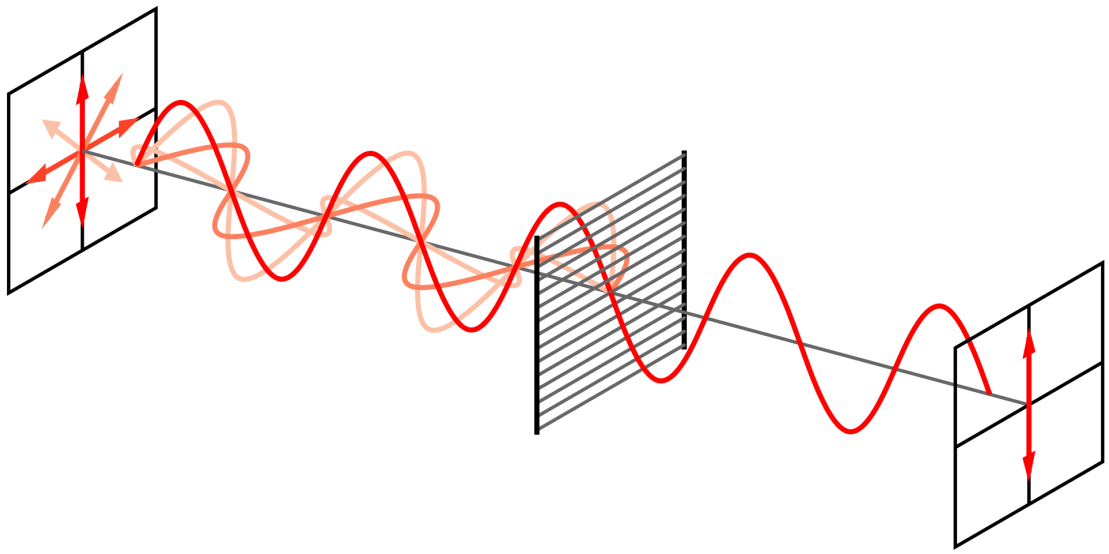

Figure 2.1. Linear polarization of incoming transverse light [14]

Different polarization states can be described mathematically based on the different directional components of the wave. Equation 2.1 describes both the x and y

components of the electric field in the z direction of propagation. With linear polarization, the electric field has a linear projection in the xy plane, this is seen when $\phi = 2\pi n(n = 0, 1, 2,)$.

$$\begin{aligned} E_x(z,t) &= iE_{0x}cos(kz - wt) \\ E_y(z,t) &= iE_{0y}cos(kz - wt + \phi) \end{aligned} \tag{2.1}$$

2.2 Polarimetric Imaging

Polarimetric imaging takes advantage of one of the characteristics of electromagnetic radiation, polarization state. When describing the features measured by an image detector there are four significant characteristics, intensity, wavelength, coherence and polarization. Most spectral sensors measure the intensity of radiation over a specified wave band or several wave bands; this information gives the user information about the distribution of matter in the scene. Polarimetry measures the nature of the radiation vector of the optical field across the scene. Polarization data tells the user about the surface features, shape, shading and texture providing information that is largely unseen in spectral imaging and thus greatly enhancing the overall information collected [2].

In order to collect this type of information a sensor must be able to capture the same image in multiple polarization states, preferably at the same time, in order to compare the different vector fields in the optical field. Several different methods have been employed in the past to accomplish this task, including a system similar to the one below in Fig. 2.2, which shows a rotating ring of linearly polarized lenses in front a stationary camera. This type of system can allow the user to collect polarimetric data, but has some severe limitations. The system must remain stationary while collecting images and the achievable frame rates are far too low for moving objects, due to the limited rotational speed of the polarizers. In addition the rotation can also cause misalignment errors with the sensor [15].

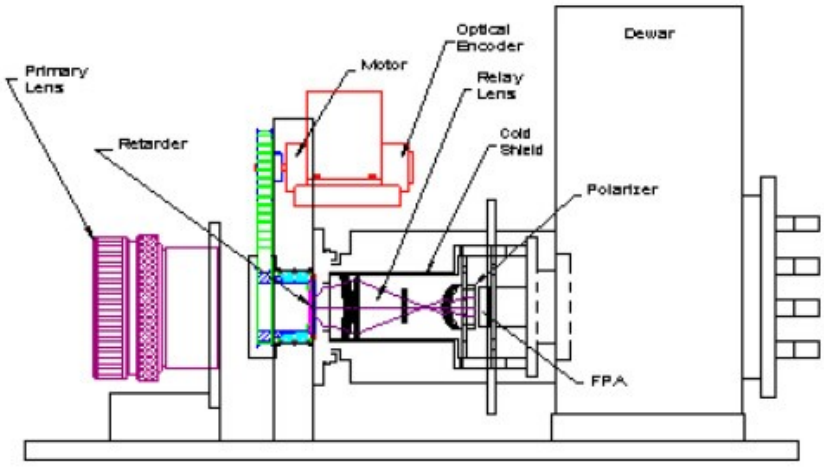

Figure 2.2. Traditional polarimetric imaging system with rotating polarizer array wheel [16]

2.3 Sub Wavelength Linear Grid Polarizer

Subwavelength linear polarizers consist of a grid of lines spaced closer together than the desired polarized wavelength. The grating structures are made of a dielectric material and then coated with a conductive top layer such as Al, Au, or Ag. As the incoming light strikes the polarizer, the transverse electric (TE) and the transverse magnetic (TM) waves are reflected and transmitted, respectively. TE and TM are parallel and perpendicular to the grating direction, respectively. A diagram of the wire grid polarizer is shown in Fig. 2.3 [17].

To understand how the wire grid polarizer selectively transmits one polarization but reflects the other, the electron movement of the incident light must be considered. If the incident light is polarized parallel to the grating (TE) then the coherent electrons will be conducted along the surface of the wires with unrestricted movement, causing the light to interact with the whole of the wire grid as a homogeneous reflective surface, similar to a metal sheet. As the electrons propagate in both directions along the line they generate an electric wave form, the forward moving wave cancels exactly the incident wave in the backward direction through deconstructive interfer-

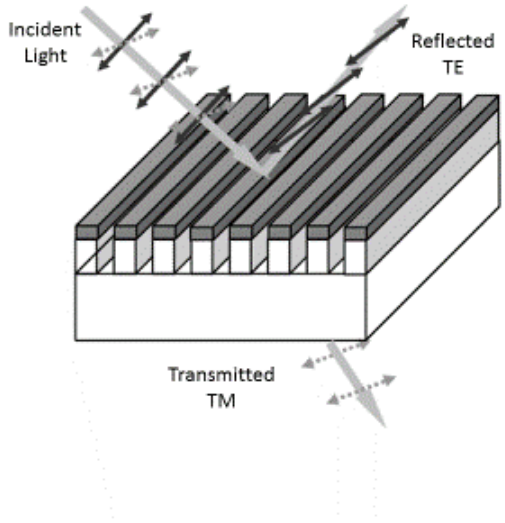

Figure 2.3. TM and TE wave transmission for wire grid polarizer [18]

ence, resulting in full reflection of the incident TE wave and no propagation of the incoming wave through the grating structure [19, 20].

Conversely, if the incident light is polarized perpendicular to the grating TM and the spacing of the grating is greater than the wavelength, then the electron movement is confined and the electron field generated in not strong enough to overcome the incident light in the forward direction, allowing high transmission and the low reflectance. In this orientation, the wire grid behaves as dielectric rather than a metal sheet and allows the transmission of TM polarized light [7, 21].

This type of polarizer is especially useful because the transmitter wavelength can be tuned by changing the dimensions of the line spacing and grid. In addition, this type of polarizer is a nanoscale film that can be directly integrated into current semiconductor production without difficulty [22].

2.4 Surface Plasmonics

Surface plasmon (SP) are induced by the oscillation of free surface electrons and the electromagnetic wave. SP induction is the method in which electrons propagate along the linear grids, as described in the previous section. More specifically, surface plasmon polarization (SPP) is the oscillation of free electrons along the conductive linear surface. Solving for the electron energy based on Maxwells equations gives the SP dispersion relation seen in equation 2.2 [20, 23].

$$K_{sp} = K_0 \sqrt{\frac{\varepsilon_d \varepsilon_m}{\varepsilon_d + \varepsilon_m}} \tag{2.2}$$

K_{sp} is the frequency dependent SP wave vector; ε_m is the frequency dependent permittivity of the metal, ε_d, is the frequency dependent permittivity of the dielectric material and K_0 is the free space wave vector. When K_{sp} is greater than K_0 there is a momentum mismatch that must be overcome in order to create the SP. Subwavelength wire gratings enable the incident light to be momentum matched by the scattering of light between the gratings periodic structure, creating SPP along the metallic lines. Due to the multiple slits in the linear grid, incident light is efficiently coupled into SP modes through momentum matching by diffraction [24]. Equation 2.3 describes this relationship with the addition of the reciprocal wave vector $G = i2\pi/p$. Where θ is the incident angle, i is the integer and p is the pitch of the metallic grating.

$$K_{spp} = K_0 \sin(\theta x) + \frac{i2\pi}{p} x \tag{2.3}$$

When rewriting equation 2.3 for normal incident ($\theta = 0$) the equation can be simplified to the following equation 2.5,2.4.

$$K_{spp} = \frac{i2\pi}{p} \tag{2.4}$$

$$\lambda_{spp} = \frac{2\pi np}{i2\pi} = \frac{np}{i} \tag{2.5}$$

Where n is the refractive index of the dielectric material and λ_{spp} is the wavelength of the SPP. In this way the periodic oscillation of the SPP resonance can be seen, the first occurring at $\lambda_{spp} = np$, and then repeated at $\lambda_{spp} = \frac{np}{k}$ for $(k = 1, 2, 3...)$ [25].

3. MATERIALS AND APPARATUS

3.1 Sulfur Polymer

As an alternative to traditional optical materials, sulfur composite organic materials have been investigated and synthesized to overcome some of the disadvantages of traditional inorganic materials. Sulfur in crystal form consists mainly of eight bond rings (cyclic octatomic molecules) which when heated will break and form a sulfur polymer matrix [26]. By crosslinking the sulfur chains while in polymer form, the sulfur is stabilized in its polymer state; this process has been termed inverse vulcanization [27]. This new sulfur polymer consists of two materials, sulfur polymer chains as the matrix and DIB as the crosslinking agent. By varying the ratio of sulfur to DIB the optical properties (index of refraction) of the material can be shifted.

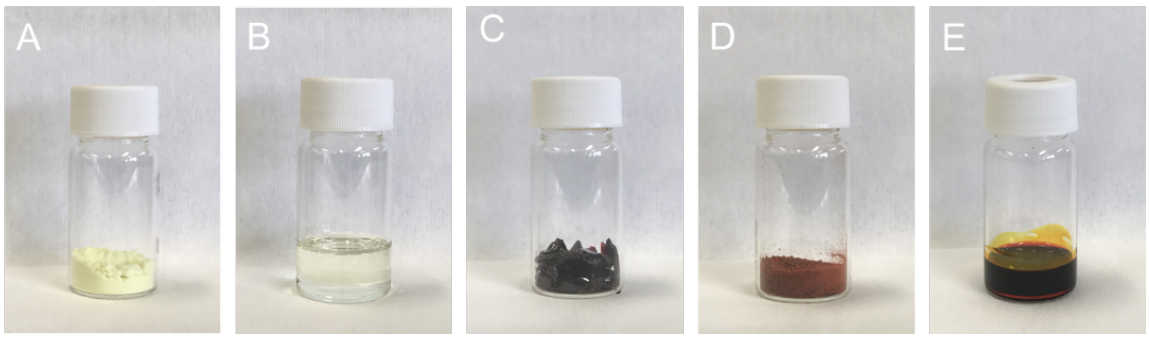

Figure 3.1. Different phases of sulfur polymer: (A), Elemental sulfur. (B), DIB. (C), Solid sulfur polymer after fabrication. (D), Ground sulfur polymer. (E), Ground sulfur polymer dissolved in 1,2-Dichlorobenzene (1g:1ml).

Fig. 3.1 shows the different physical states of sulfur polymer throughout the fabrication process. Fig. 3.1 (A) shows Elemental S (MW =32.07 g/mol) obtained from Sigma Aldrich, which was used without further treatment. Fig. 3.1 (B) is

the crosslinking agent, 1-3, Dissopropenylbenzene (DIB, MW:158.24 g/mol, Sigma Aldric). Fig. 3.1 (C) is sulfur polymer 35 percent weight sulfur, 65 percent weight DIB and Fig. 3.1 (D) is the same polymer ground into powder and Fig. 3.1 (E) the powder was dissolved in one ml of dichlorobenzene per one gram powdered sulfur polymer (MW: 147.00 g/mol, Sigma Aldrich).

Past work has shown the feasibility of sulfur composite for IR imaging lenses [10], cathode material in LiS batteries [28] and nano pillar grating [27]. Previous testing of free standing films of sulfur copolymer shows the distinct shift in index of refraction as the sulfur content is varied in the composite. This new copolymer material has the ability to be drop cast or thermally molded; thermal annealing and surface repair have also been demonstrated [29]. Thermal molding and injection molding have been used as economic fabrication process for polymer optics. Injection molding allows for the incorporation of the optical surface and mounting features all in one part, without costly grinding and polishing steps found in the fabrication of traditional IR optics [30]. With the advantages of copolymer fabrication versus traditional inorganic glass fabrication being so great, sulfur copolymer is a useful IR optical component.

3.2 Mold Fabrication

In order to create a polymer based linear grating a suitable fabrication method must first be determined. For this thesis, NIL was chosen as the preferred fabrication method to create the test samples. NIL is a well understood fabrication method that has the ability to be scaled up in the future to industrial production levels of manufacturing. The NIL process is briefly described in Fig. 3.2. A mold was used to imprint the desired pattern into the polymer material, the polymer is cured with the mold in place, the polymer was allowed to cool and then the mold was removed, leaving the desired pattern transferred into the polymer material on the Si substrate. Creating the master mold that allowed imprint molds to be cast was the first step in preparing this type of fabrication.

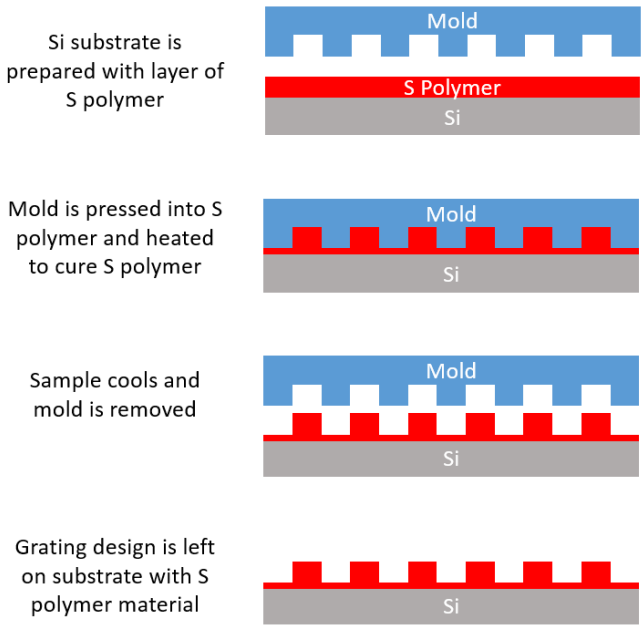

Figure 3.2. NIL diagram for the sulfur polymer based polarizer samples

The following three subsections will cover in detail the master mold fabrication process for the subwavelength grating: 1) linear grating design, 2) electron beam lithography (EBL), and 3) reactive ion etching (RIE). The first step was to design the grating structure desired for the polarizer. The parameters for this include the height, width and pitch of the linear grids. All these parameters have an effect on the performance of the polarizer and the target wavelength.

After the design step, the master mold was fabricated to the desired dimensions. To create a master mold several processes were used including electron beam lithography, chemical vapor deposition and reactive ion etching.

3.2.1 Linear Grating Design

Initial simulation was completed to evaluate the performance of different grating structures and layouts. As seen below in Fig. 3.3. Four different grating structures

were considered, (A) a conductive single layer wire grating with no sulfur polymer dielectric layer, (B) a conductive single layer wire grating with a sulfur polymer dielectric layer, (C) a conductive two layer wire grating with no sulfur polymer dielectric layer on the lower layer, and (D) a conductive two layer wire grating with sulfur polymer dielectric layer under both layers.

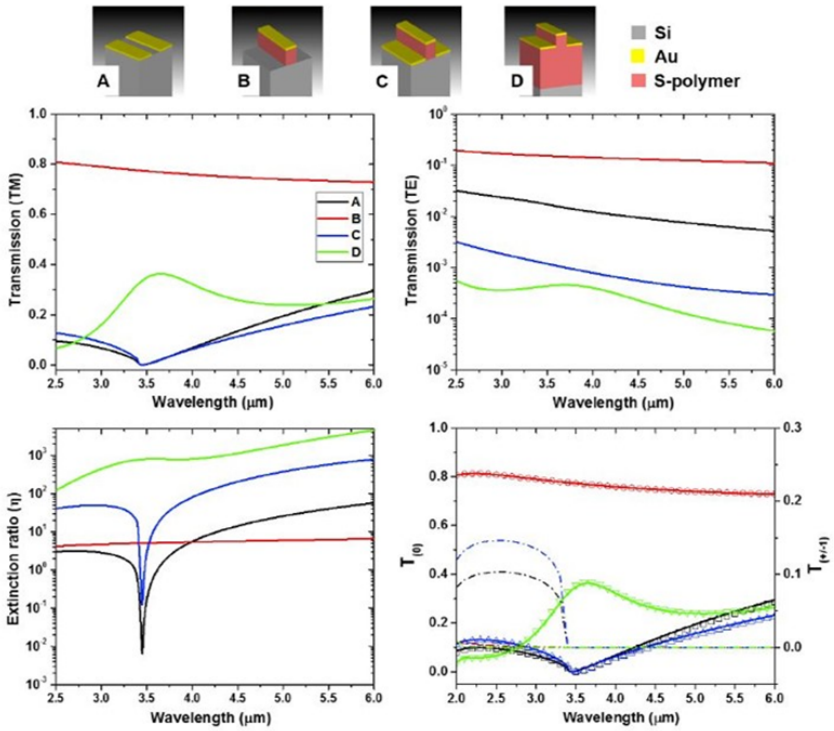

Figure 3.3. Variable Model Simulation Results: (Four models are compared in the figure, (A) single layer gold grating, (B) single layer gold on sulfur polymer pillar, (C) bilayer gold on sulfur polymer pillar, (D) bi-layer gold on sulfur polymer pillar and substrate), (a), TM transmission. (b), TE transmission. (c), Extinction ratio. (d), Phase transmission.

Fig. 3.3 show the highest transmission of TM light for sample (B) but sample (B) also has the highest TE transmission meaning there is low selectivity for this polarizer design and low extinction ratio. Samples (A) and (C) both show lower TM transmission and TE transmission, including a dip in TM transmission at 3.5μm, also reflected in the extinction ratio. Sample (D) has the best results and reflects the

final design used, with high TM transmission and low TE values. In addition, sample (D) has a positive peak at 3.5μm caused by the Fabry–Pérot constructive resonance between the multi-layer structure.

Based on equation 2.5 to solve for the surface plasmon frequency, and the design simulation in Fig. 3.3, the parameters for the linear gratings had been determined to be as shown in table 3.1 below. Each variable corresponds to a dimension of the grating design displayed in Fig. 3.4 below.

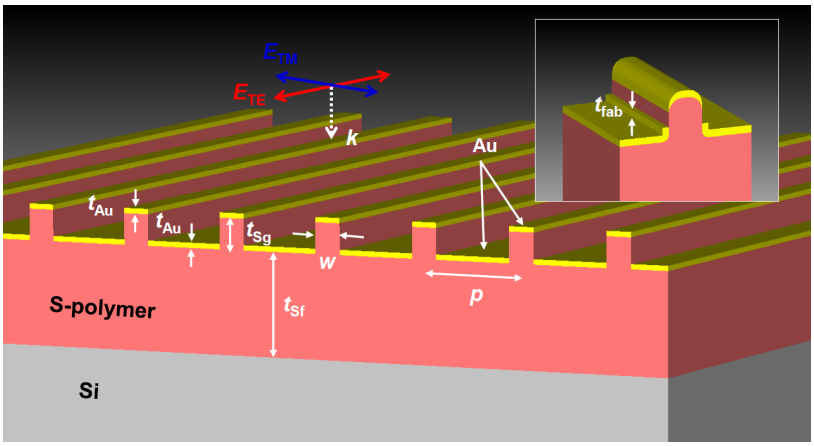

Figure 3.4. Diagram of dimension variables for wire grid polarizer design

Table 3.1. Ideal grating design parameters

Design Parameters					
Variable	t_{Au}	t_{Sg}	t_{Sf}	w	p
Sample 1	50 nm	300 nm	1000 nm	300 nm	1000 nm
Sample 2	50 nm	300 nm	1000 nm	490 nm	700 nm

The design above in Fig. 3.4 displays the ideal dimensions of the fabricated sample as determined by the simulation shown in Fig. 3.3, these dimensions were used to design the master mold. The master mold was then used to cast the NIL molds for sample fabrication. If the final design was considered the positive profile, then the

mold used to imprint that design would be considered the negative profile and if the negative profile mold was cast from a master mold then that master mold would have to be the positive profile of the design. This pattern design transfer is explained visually in Fig. 3.5 below.

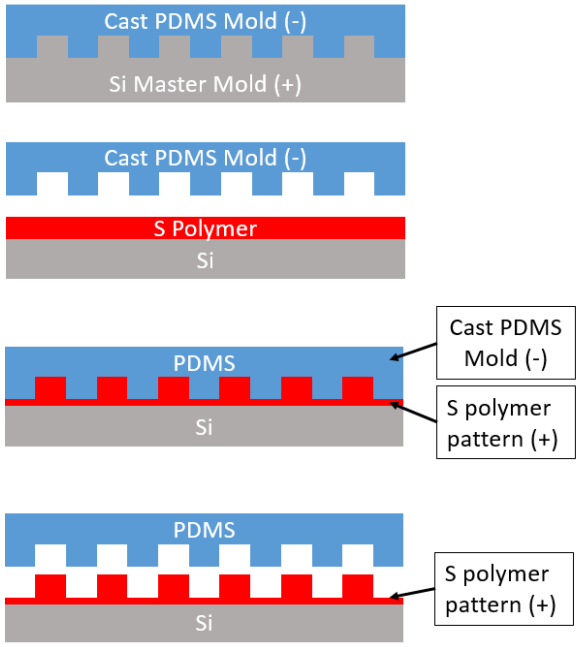

Figure 3.5. NIL diagram for the sulfur polymer based polarizer samples. Positive and negative molds

Now, understanding the pattern transferring process, the master mold was designed to ensure a correct final sample with appropriate dimensions. The design for the master mold was used for electron beam lithography and needed to show where the photoresist was removed. An image of a section of the master mold design is displayed below in Fig. 3.6 in the file format GDS, which is read by the electron beam lithography system. The mold total size was set to 5mm by 5mm due to time constraints from the fabrication steps.

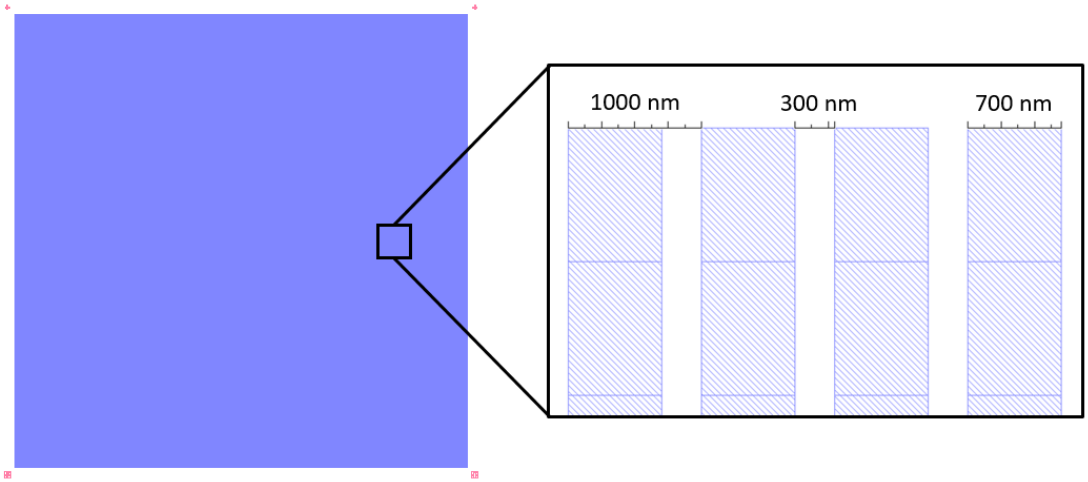

Figure 3.6. GDS file image for use in E-Beam lithography

3.2.2 Electron Beam Lithography

With the grating design complete and the master mold design created, the next step was to begin the fabrication of the Si master mold. This mold was used multiple times for casting molds to make the linear grating samples. To physically withstand the multiple casting cycles the master mold was made from Si; the design was etched into the surface by reactive ion etching using a sacrificial photopolymer mask. The sacrificial mask was the next part of the fabrication and was created with electron beam lithography.

Fig. 3.7 shows the process of Si etching, the first four steps are a part of the EBL process. A silicon wafer was chosen as the substrate material because it was easy to etch and readily available. The wafer was purchased with a 100nm wet thermal silicon oxide layer grown on the surface. Once received, the wafer was cleaned with IPA and then a vapor prime process was applied to the wafer's surface to enhance the contact strength of the photoresist. After vapor prime, a positive photoresist, GL-2000M, was spun onto the surface of the wafer creating a thin film of constant

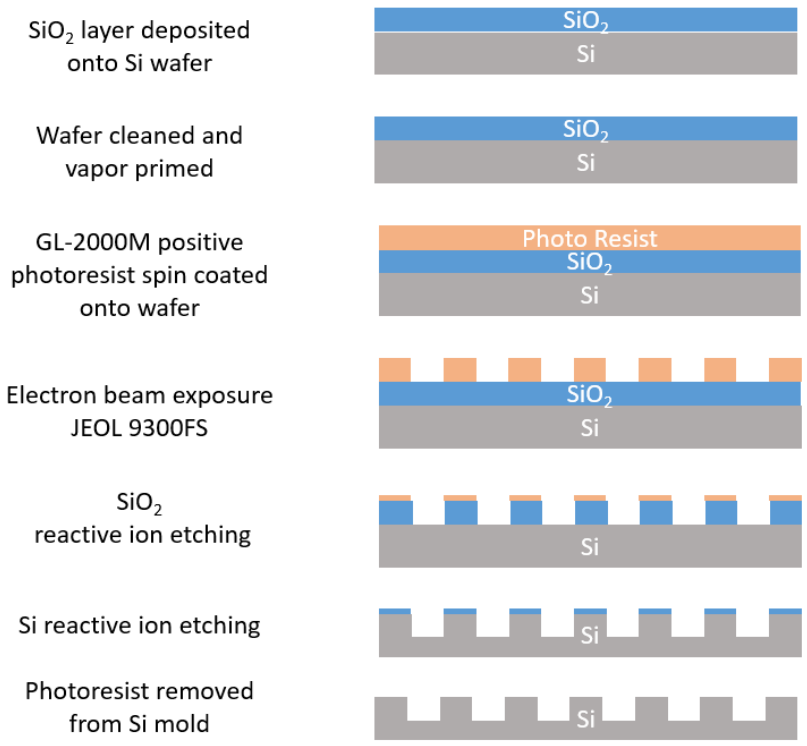

Figure 3.7. Si master mold fabrication steps

thickness. The GL-2000M photoresist layer was then cured by setting the wafer on a hot plate at 150^{o}C for 3 minutes, then slowly cooled to reduce internal stresses caused by sudden shrinking. At this point the wafer was fully prepared and ready for electron beam writing.

The positive photoresist was fully cured across the surface of the wafer and selective exposed by an electron beam to create the desired pattern inside the JEOL 9300FS e-beam lithography system. The photoresist was broken down where the electron beam struck and allowed the electron beam to trace the design into the photoresist layer. The electron beam traced the linear grid pattern onto the wafer in accordance with the design file depicted in Fig. 3.6. After several hours, the electron beam exposure was complete and the sample was removed from the JEOL 9300.

With the exposure complete, the grating design then needed to be developed. The sample was immersed in a bath of N-amyl-acetate for 30 seconds to remove all the photoresist that had been broken down by the electron beam exposure. The sample was then rinsed in isopropyl alcohol (IPA) to stop the development process and then placed in a bath of IPA to remove any excess photoresist left behind. At this stage the grating pattern was checked for defects with a microscope, as shown in the image in Fig. 3.8 along with a diagram of the material layer structure in cross section.

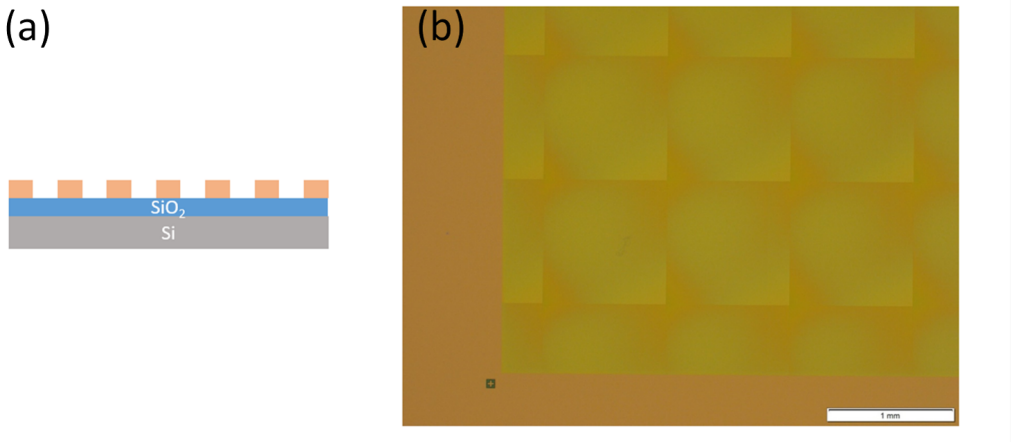

Figure 3.8. (a) Cross sectional diagram of sample (b) Optical microscope image of mold after E-beam writing is complete

If the sacrificial photopolymer mask showed no defects then the EBL process was successful. With success, the EBL process was now complete and the mold needed only to be etched in order to be complete and ready for dimensional validation.

3.2.3 Reactive Ion Etching

Reactive ion etching (RIE) is a fabrication process that removes varied materials at different rates depending on the gaseous ions used during the process. The sample to be etched will be placed inside an RIE chamber and an etching gas will be pumped

in while the chamber reaches a low vacuum. Once the desired pressure is reached, a radio frequency electromagnetic field is applied to the electrode to induces a plasma field by oscillating the electric field and ionizing the gas, thus freeing the electrons. As the electrons travel up and down in the electromagnetic field they are discharged to ground at the upper wall of the chamber, and collect at the base of the chamber thus creating a negative charge at the base of the chamber. The negative charge at the base of the chamber attracts the positive gas ions, causing them to collide with the sample at the base of the chamber. By selecting the right etching gas the ion bombardment will react with the surface of the sample and create a volatile byproduct that can be pumped out. Due to the directional bombardment of the ions this etching process is anisotropic [31]. Fig. 3.9 illustrates this concept, showing the induced plasma, ion bombardment and etchant byproduct.

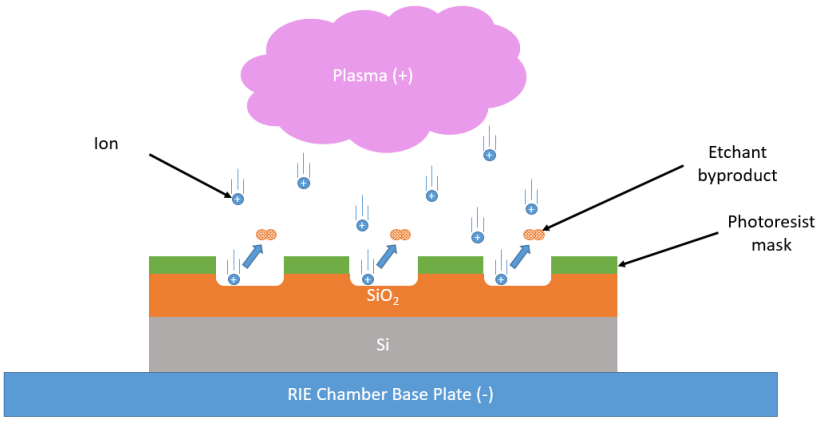

Figure 3.9. Reactive ion etching diagram

For the master mold sample, two different etching steps were required using two different gas mixtures. The first step was to selectively etch the SiO_2 layer down to the Si layer in the pattern of the photoresist mask. This process required a mixture of O_2 and CHF_3 as the etchant gas to etch the SiO_2, with an etch byproducts of SiF_4, CO and O. After this step, the sample has gone from Fig. 3.10 (A) to Fig. 3.10 (B).

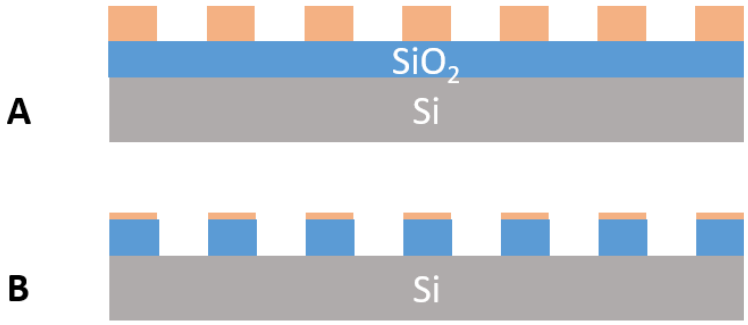

Figure 3.10. SiO_2 etching process

The second step in the RIE process was to selectively etch the Si layer to form the pattern of the photoresist mask into the Si wafer. This process required a mixture of O_2 and CF_4 as the etchant gas to etch the Si, with a etch byproduct of SiF_4. After this step, the sample has gone from Fig. 3.11 (A) to Fig. 3.11 (B).

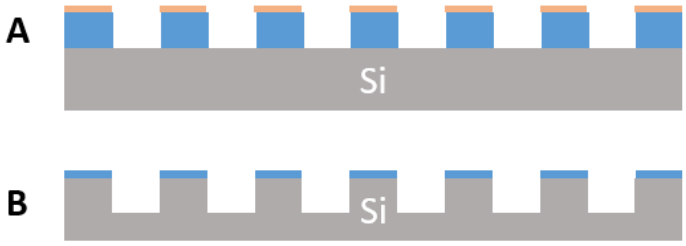

Figure 3.11. Si etching process

At this stage the master mold pattern had been successfully transferred into the Si wafer. A final etching step was applied to remove the residual SiO_2 on the surface of the master mold. Cross sectional scanning electron microscopy (SEM) is the most efficient method of validating the mold dimensions but it is a destructive test,

requiring a cut through the mold grating. To avoid this, a copy of the master mold was made from OrmoStamp with the inverse profile of the master mold. This copy was then cut, and SEM examination was performed to confirm the dimensions of the master mold, as shown in Fig. 3.12.

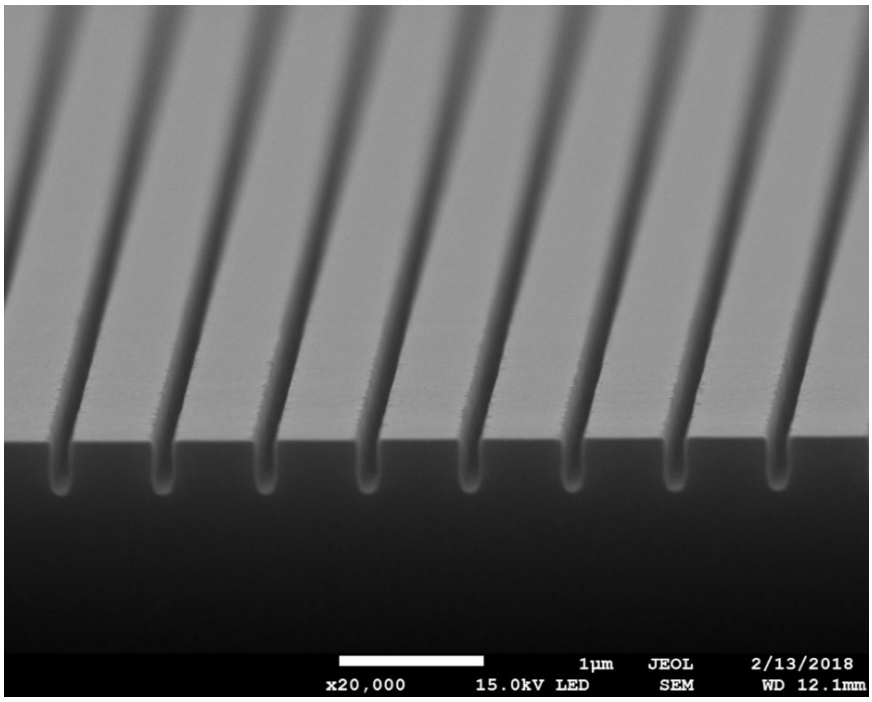

Figure 3.12. Cross sectional SEM of 700nm pitch master mold copy in OrmoStamp

3.3 Sample Fabrication

With the master mold complete the PDMS stamp was then cast. The master mold was treated with a hydrophobic surfactant (F13-TCS, 1H, 1H, 2H, 2H perfluorooctyl-trichlorosilane) in a vapor chamber to create a hydrophobic surface which allowed easy removal of the cast PDMS. After the hydrophobic coating, PDMS was mixed, the PDMS was then degassed and cast onto the master mold. The PDMS cured overnight at 150^{o}C and was then removed from the master mold surface by separating

the mold and stamp. The PDMS stamp was then treated with the same hydrophobic surfactant used on the master mold.

Double side polished Si wafer was the chosen material substrate for the polymer grating because it is transparent in the desired wavelength as well as being an easily obtained and processed material. The Si wafer was cut to size (approximately 2cm square sections) and cleaned in preparation for spin coating.

To allow for spin coating, the polymer material must first be dissolved in a carrier solvent. For sulfur polymer the chosen solvent was 1-2 dichlorobenzene (DIC). Sulfur polymer was finely ground and dissolved in the solvent at 1g polymer to 1ml solvent ratio. The mixture was stirred and heated to 125^{o}C, just below the glass transition temperature (T_g) of the sulfur polymer material, to insure complete dissolution in the solvent.

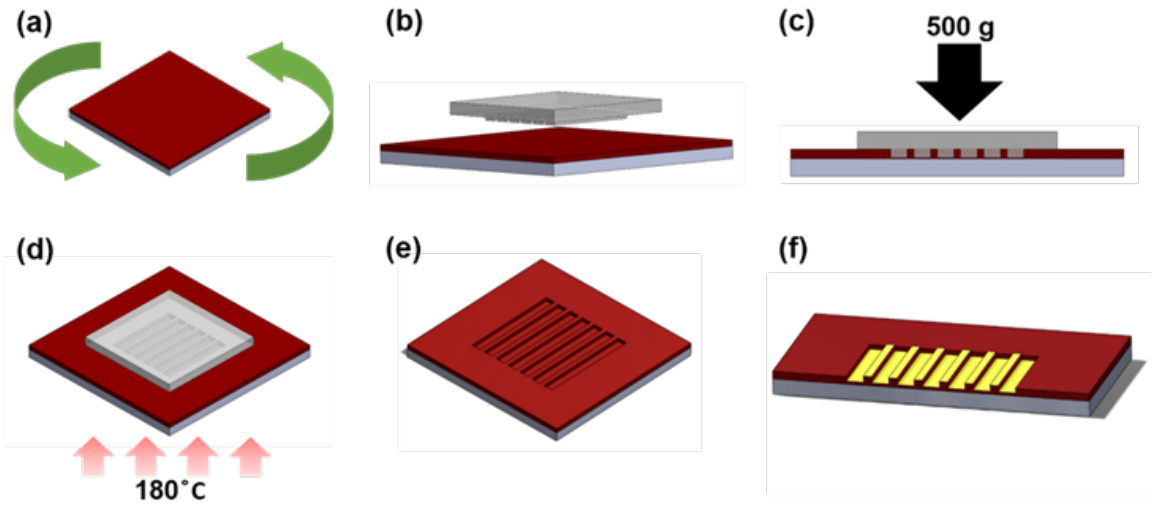

Figure 3.13. (a), Wafer is spin coated with dissolved polymer. (b), PDMS stamp is aligned over coated wafer. (c), Stamp is mechanically pressed into liquid polymer. (d), Stamp and wafer are heated to solidify polymer structure. (e), Stamp is removed leaving sulfur polymer structure. (f), Gold is deposited on horizontal surfaces 50nm thickness.

With the cleaned wafers and dissolved polymer, the spin coating process was prepared. The Si wafer was loaded onto the spin coater and the polymer material pressed through a 0.2μm syringe filter and deposited onto the wafer surface. Spinning at 2000 rpm for 7 seconds with an acceleration of 1000 rps^2. Created a level layer of sulfur polymer across the surface of the wafer. This process was repeated a second time to create a thicker polymer film. This step is shown in Fig. 3.13 (A).

The uncured polymer film was then imprinted with the PDMS mold and a weight of 500g was applied to the stamp to maintain pressure on the mold as shown in Fig. 3.13 (B, C). To cure the polymer, the carrier solvent has to be removed; in this case the solvent was evaporated in an oven at 180^{o}C for 20 minutes. After the carrier solvent is evaporated the polymer was still soft due to the high temperature and was allowed to cool before the stamp was removed, as shown in Fig. 3.13 (D). After cooling and stamp removal the linear grating pattern can easily be seen in the sulfur polymer, illustrated in Fig. 3.13 (E).

To complete the sample fabrication a thin layer of conductive material was applied to the horizontal surfaces of the grating in order to allow for the conduction of TE direction radiation. Metal deposition was applied with an electron beam evaporation system (Temscal FC-2000, Ferrotec) at a pressure of 4x10^{-7}Torr. At this pressure and with a normal incident the deposition can be considered non-divergent and will only coat the horizontal surfaces of the grating, leaving the sidewalls of sulfur polymer uncoated [32]. An 5 nm thick adhesion layer of Cr was first applied and then 50 nm of Au was evaporated onto the surface of the sample, completing the fabrication. This final step is shown in Fig. 3.13 (F).

4. PHYSICAL TESTING

4.1 IR-VASE Ellipsometry

Ellipsometry is a tool used to gain information about the optical constants of materials. The ellipsometer generates a light beam with a known polarization state and reflects that beam off the sample surface. As the beam passes through the sample the polarization state changes and the reflection angle changes. The beam is then measured by a detector and the new polarization state of the beam is measured and compared to the original input. Two terms are measured by the ellipsometer: Psi (Ψ) is a measurement of the ratio of the amplitude diminutions ranging from 0^o-90^o, and delta (Δ) is the phase difference between the input and output beam. From these two measured terms, a model-based analysis can be fit based on the governing equations describing the interaction of light passing through different materials.

The sulfur polymer was measured with an IR-VASE ellipsometer (J.A. Woollam) with 35 percent sulfur and 70 percent sulfur polymer samples. The samples were prepared as thin films on single side polished Si wafers, with constant film thickness of 5μm; measurements were taken from several angles, including 65^o, 70^o, and 75^o. With several different angles of measurements, the fitting of the analysis model was improved and an estimate of the film thickness was achieved by comparing the reflection path measured at the different angels.

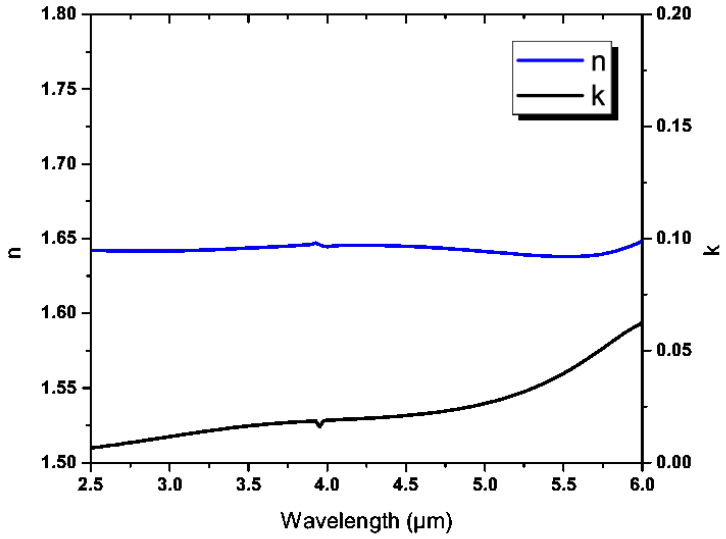

Figure 4.1. Ellipsometry results for 35 percent sulfur thin film sample, (n) refractive index, (k) extinction coefficient

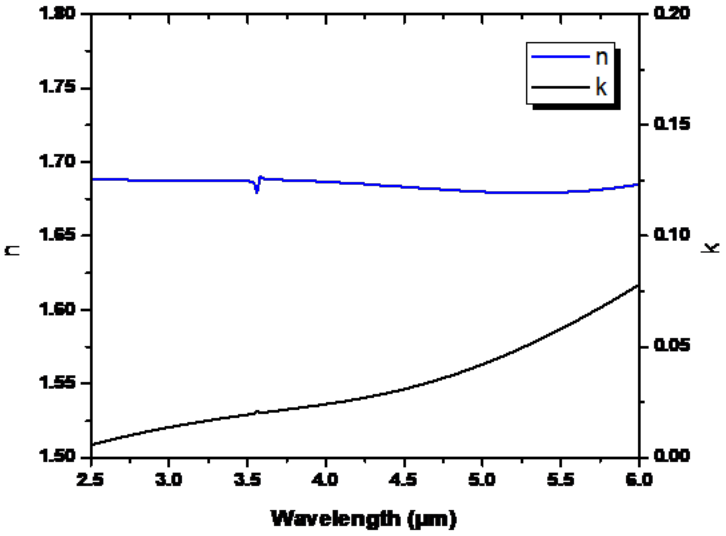

Figure 4.2. Ellipsometry results for 70 percent sulfur thin film sample, (n) refractive index, (k) extinction coefficient

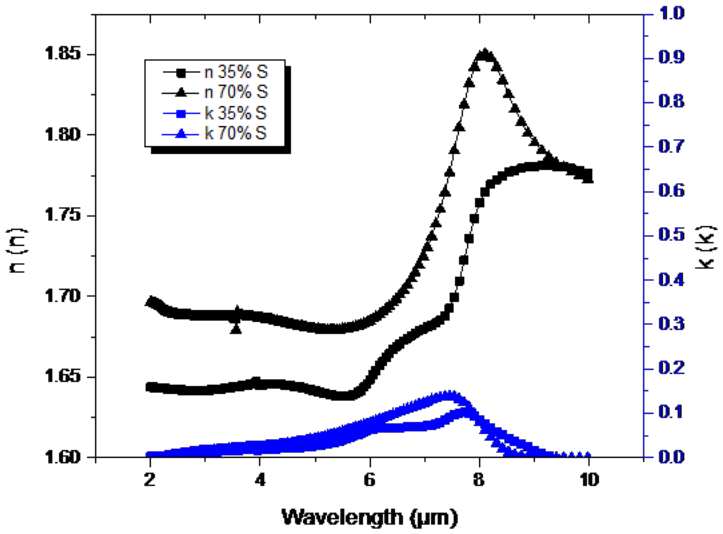

Figure 4.3. Ellipsometry results for 35 percent sulfur and 70 percent sulfur thin film sample, n refractive index, k extinction coefficient

The n and k values of 35 percent sulfur are shown in Fig. 4.1 The index of refraction for this polymer is 1.64 through the range of 2.5-6 μm and has a low extinction coefficient. The extinction coefficient measures the attenuation level of an electromagnetic beam as it travels through the measured material [33]. Fig. 4.1 shows that the 35 percent sulfur polymer has a extinction ratio in the range of 0-0.6, which is higher that standard MIR materials and is an area in need of improvement for sulfur based polymer. Fig. 4.2 shows the refractive index of the 70 percent sulfur polymer has a positive index shift to 1.68, as compared to the 35 percent sulfur polymer. By varying the sulfur to DIB ratio the optical properties of the polymer can be modified, Fig. 4.3 shows the n and k values of 35 percent sulfur and 70 percent sulfur polymer in the same figure. The increase in the refractive index is visible from 35 percent sulfur to 70 percent sulfur, showing that with a higher sulfur content the refractive index will increase. The shift to the positive index is due to the reduction of C-H and C-O bonds in the polymer and an increase in S-S bonds. The absorption peaks of C-H and C-O bonds fall directly in the MIR range (3.3μm) and (5.7μm) respectively,

while the absorption peaks of S-S bonds are much further out into the far IR at (15μm) [34, 35].

4.2 FRIT Transmission

The grating sample was checked for polarization performance with FTIR, by comparing the TM and TE transmission. Before the sample was tested, a duplicate sample was cut in half and examined via cross-sectional SEM to verify the geometry of the grating. As shown in Fig. 4.4, the grating height is 296nm, the sulfur substrate thickness was 900nm, and the gold layer deposition was on only the horizontal surfaces. There was some rounding of the gold layer on the upper edges of the gratings and some additional gold buildup in the creases of the grating corners. This imperfection in the grating fabrication limited the performance of the sample, the extent of which is shown in with simulation in the analysis section.

Testing of the linear grating polarizer performance was performed with FTIR. Transmission measurements were taken using a Fisher Scientific Nicolet iS50 FTIR over the range of 2.0-6.5 μm wavelength, with a spectral resolution of four nanometers. A commercial wire grid polarizer (Bruker) was added to the beam path after exiting the FTIR and before the grating sample and detector. The bilayer grating sample was positioned on the sample stage, with a two millimeter diameter pinhole positioned over the grating. Due to the relatively small size of the grating compared to the FTIR beam, a two millimeter pinhole was used to only allow light passing through the sample grating to be measured.

The commercial polarizer was adjusted for maximum transmission where the axis of the Bruker polarizer was parallel with the TM axis of the bilayer grating; the spectra was then measured as TM transmission. The TE direction was perpendicular to the TM, thus the Bruker polarizer was rotated 90^o and the TE transmission spectra was measured. For transmission analysis, bare double side polished Si substrates were measured with the Bruker polarizer in the same position as the single beam sample

measurement for use as background spectra. The transmission spectra for TM, TE and the extinction ratio for the sulfur polymer grating sample 1 and sample 2 are all shown in this section.

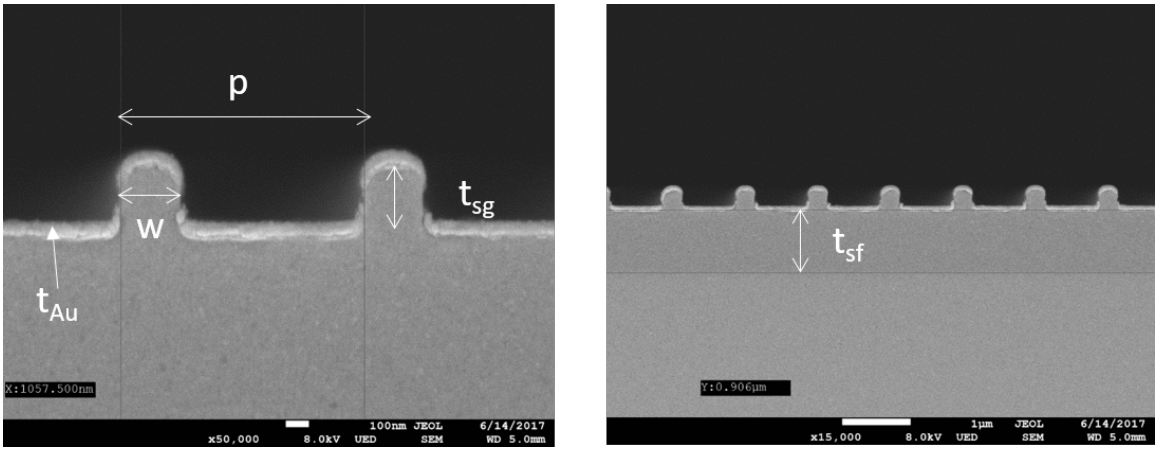

Figure 4.4. Cross sectional SEM of 1000nm pitch wire grid sample 35 percent sulfur

Table 4.1. Design dimensions and fabrication dimensions for 1000nm pitch grating sample

Dimensional Comparison of Design and Fabrication		
Dimension (nm)	Design	Fabrication
p	1000	1000
r=$\frac{w}{p}$	300	250
t_{Sg}	300	296
t_{sf}	1000	900
t_{Au}	50	50 $\approx$ 80

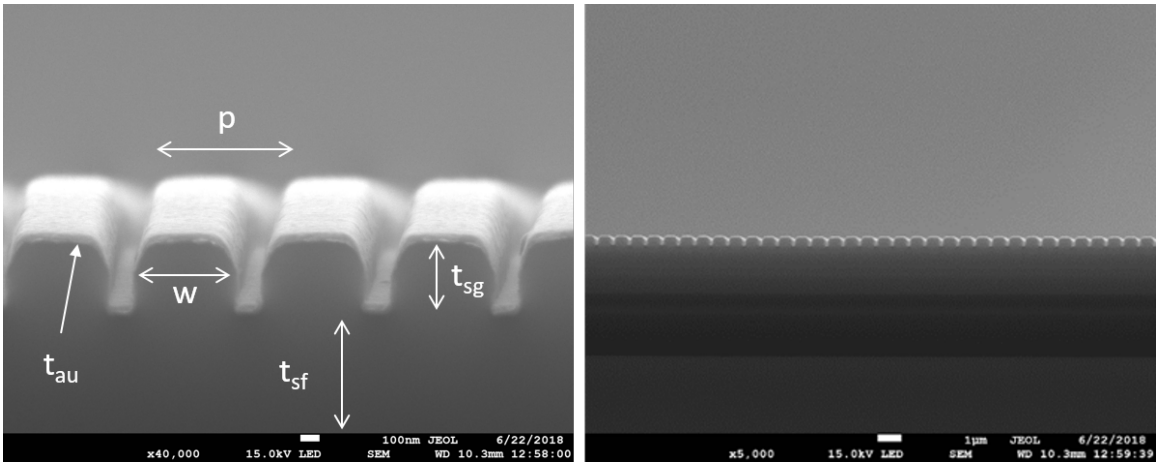

Figure 4.5. Cross sectional SEM of 700nm pitch wire grid sample 35 percent sulfur

Table 4.2. Design dimensions and fabrication dimensions for 700nm pitch grating sample

Dimensional Comparison of Design and Fabrication		
Dimension (nm)	Design	Fabrication
p	700	700
r=$\frac{w}{p}$	490	550
t_{Sg}	300	430
t_{sf}	1000	4530
t_{Au}	50	51

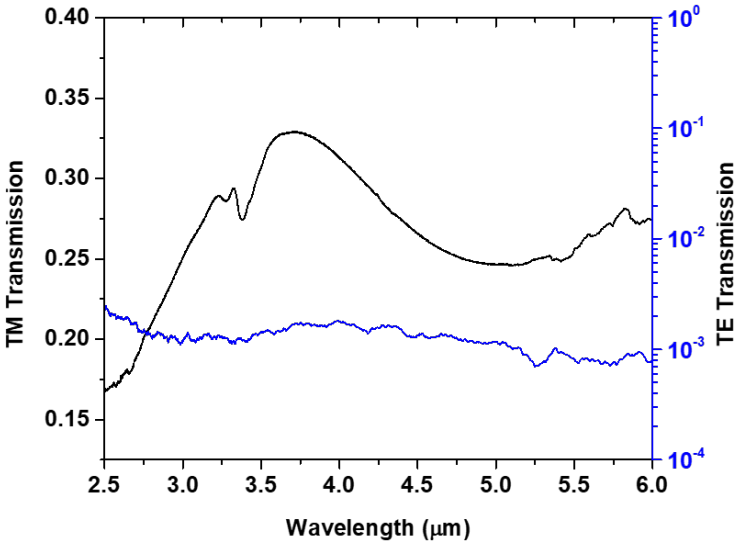

Figure 4.6. TM and TE transmission performance of 35 percent sulfur, 1000nm pitch sample

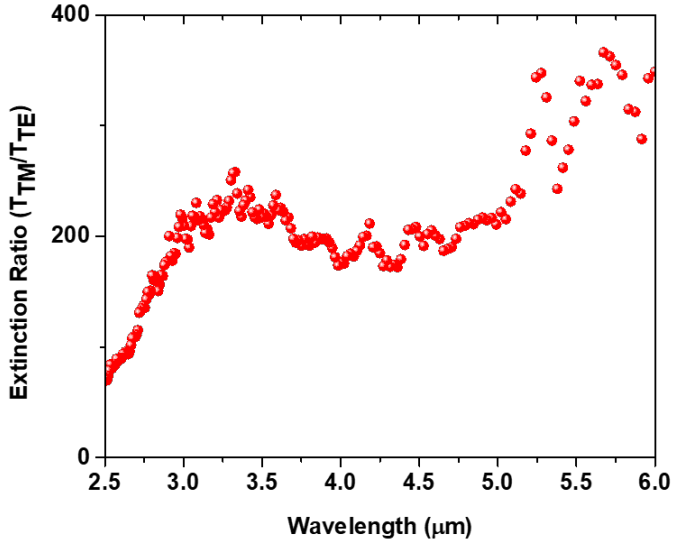

Figure 4.7. Extinction ratio performance of 35 percent sulfur, 1000 nm pitch sample

In Fig. 4.6 the TM and TE transmission is represented on the left axis while the extinction ratio (TM/TE) is shown on the right axis. The transmission data shows that the sulfur based, 1000nm pitch, MIR polarizer is viable and can function at a high extinction ratio. With TM transmission over 30 percent and an extinction ratio of over 300 (Fig. 4.7) the polarizer is viable for integration into optical systems, with the added benefit of being a low-cost polymer material. There is a single peak shown in the range of 3.5μm for TM transmission that correlates to the phase matching of the Fabry–Pérot resonance condition.

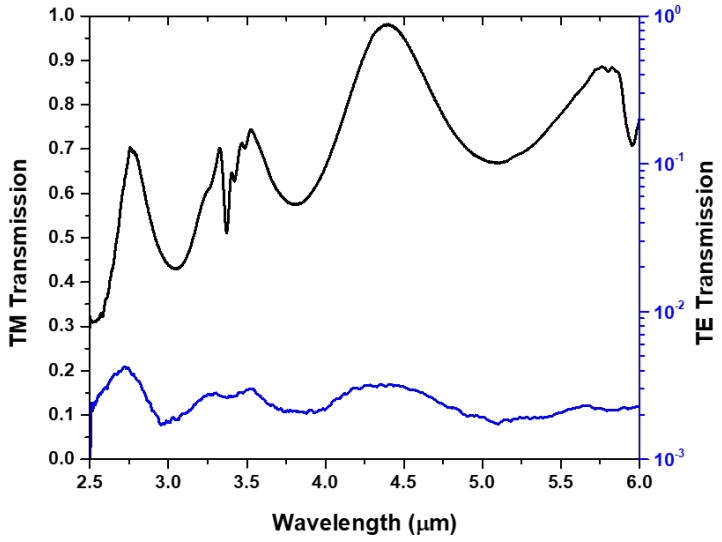

Figure 4.8. TM and TE transmission performance of 35 percent sulfur, 700 nm pitch sample

In Fig. 4.8 the TM and TE transmission is represented on the left axis while the extinction ratio (TM/TE) is shown on the right axis. The results above show that the sulfur based, 700nm pitch, MIR polarizer performed at an even higher transmission and extinction level compared to the 1000nm pitch sample. With TM transmission over 95 percent and an extinction ratio over 600 (Fig. 4.9).

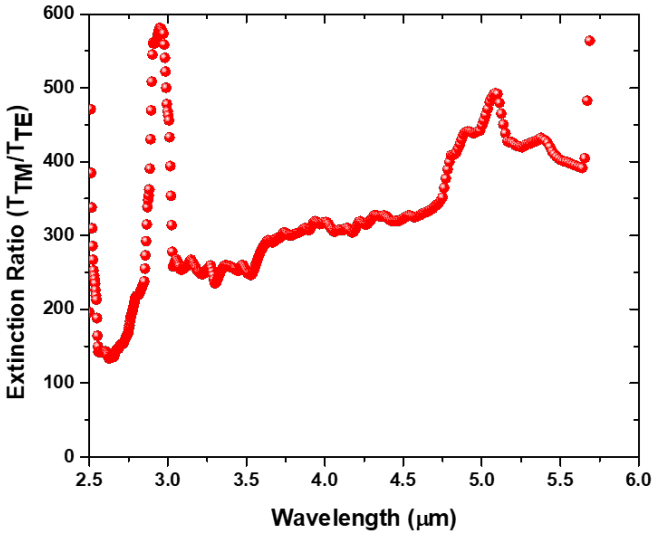

Figure 4.9. Extinction ratio performance of 35 percent sulfur, 700nm pitch sample

5. ANALYSIS

5.1 Analytical Stacked Layer Method

The stacked layer method is a simplified numerical model used to approximate the transmission performance of the wire grid structure. By solving for the reflection and transmission at each layer of the structure. The total reflectance and transmission can be solved for as the sum of all reflection and transmission in the structure [36,37]. Equations 5.2 and 5.3 show the total reflection and transmission for the three layer structure shown in Fig. 5.1 (A), with two interfaces at the junction of air and sulfur polymer and at the layer of sulfur polymer and Si wafer. Where r_{12} and r_{21} are the reflection coefficients of the bilayer Au gratings at the Layer 1 (Air) and Layer 2 (poly(S-r-DIB)) sides, respectively. Similarly, r_{23} is the reflection coefficient from the Layer 2 (poly(S-r-DIB)) to Layer 3 (Si). the propagating phase factor is β in the poly(S-r-DIB) film shown in equation 5.1.

$$\beta = n_{S-DIB} \cdot k \cdot t_{S-DIB} \tag{5.1}$$

Where n_{S-DIB}, k, and t_{S-DIB} are the refractive index of poly(S-r-DIB), the wave vector, and the thickness of the poly(S-r-DIB) layer. α is $t_{21}t_{12} - r_{21}r_{12} \approx 1$, where t_{21} and t_{12} are the forward and backward transmission coefficients through the bilayer Au gratings, respectively.

$$R = \frac{r_{12} + \alpha r_{23}\exp(-2i\beta)}{1 - r_{21}r_{23}\exp(-2i\beta)} \tag{5.2}$$

$$T = \frac{t_{12}t_{23}\exp(-i\beta)}{1 - r_{21}r_{23}\exp(-2i\beta)} \tag{5.3}$$

This computation calculation-based approach to finding the transmission and reflection highlights the type of internal interference patterns caused by the multilayer

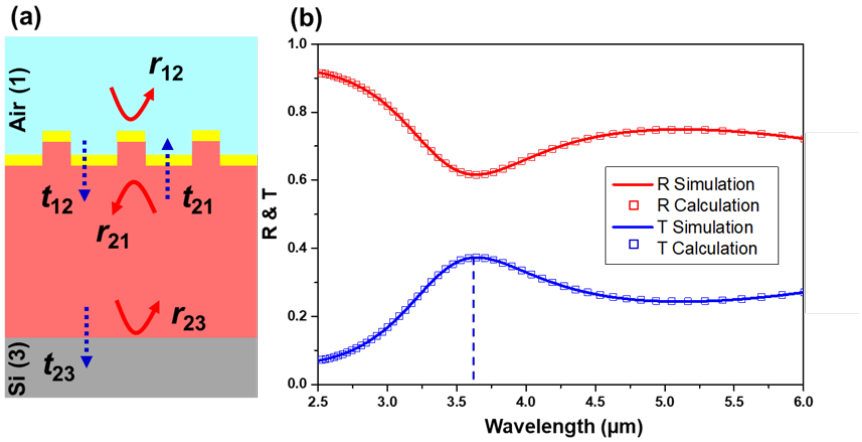

Figure 5.1. (a) Diagram of the stacked layer method, air (1), sulfur polymer (2), Si (3). (b) Comparison of total reflection and total transmission from COMSOL (simulated) and stacked layer method (calculated)

structure. The increase in transmission just past 3.5μm is attributed to the constructive interference patter in the bilayer structure known as Fabry–Pérot interference. COMSOL simulation was run on the same grating structure design shown in Fig. 5.1 (a) and the results were almost identical to those displayed in Fig. 5.1 (b) showing that the analytical model has the ability to accurately predict the transmission and reflection properties of simple geometry grating structures.

5.2 Electromagnetic Simulation

2-D simulation was used as a tool to validate and investigate the different designs of the grating structures as well as determine the cause of some of the unexpected results from experimental testing. COMSOL Multiphysics was the software used to perform all the simulations in this body of work. For initial design validation the analytical model was sufficient, but when looking at complex changes in the sample geometry from fabrication errors, a complete two dimensional electromagnetic simulation was

required for accurate results. The simulations were run with the design dimensions for each of the sample sets previously shown in table 3.1.

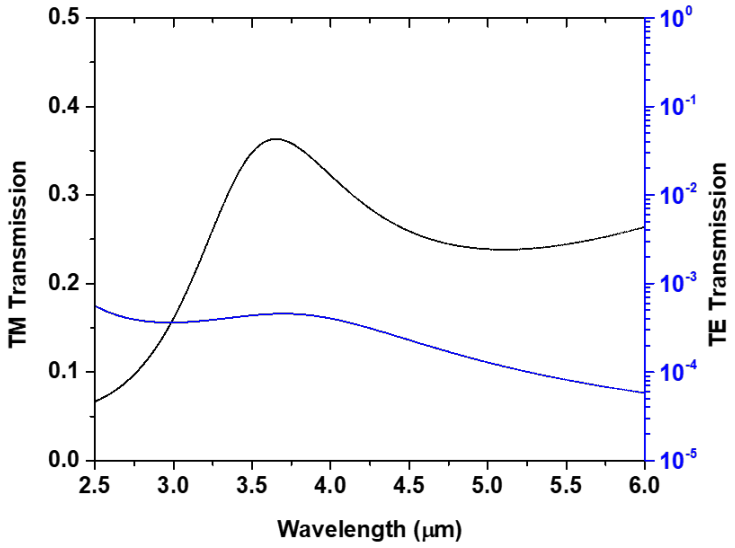

Figure 5.2. TM and TE transmission simulation of 35 percent sulfur 1000nm pitch design

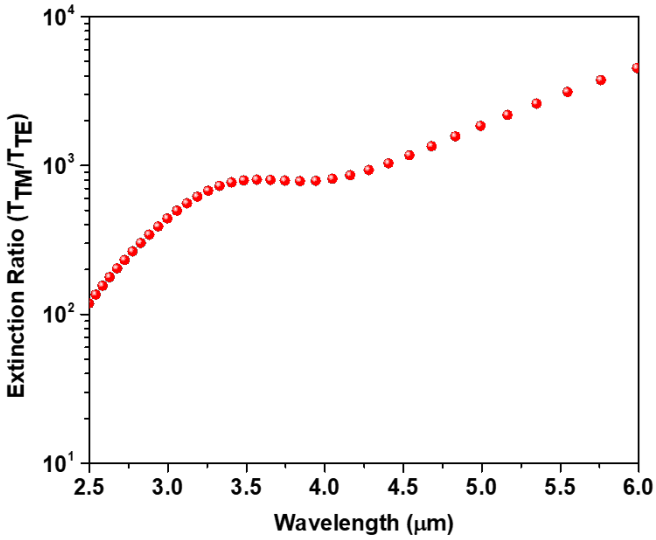

Figure 5.3. Extinction ratio simulation of 35 percent sulfur 1000nm pitch design

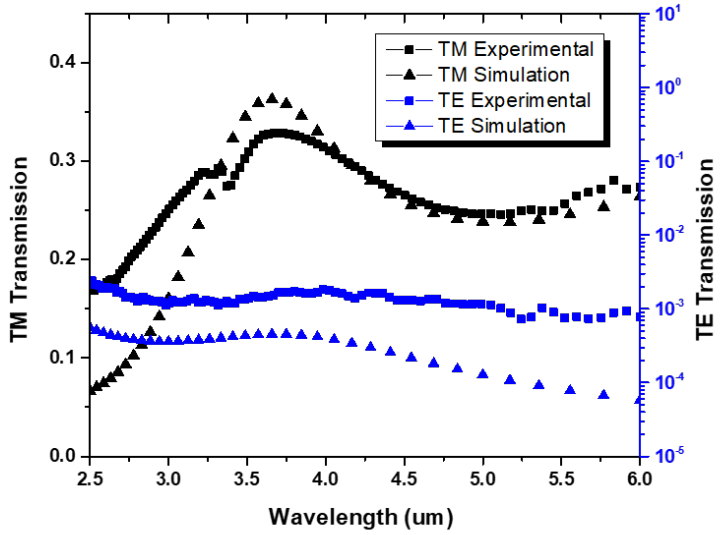

Figure 5.4. TM and TE transmission simulation and experiment results overlay of 35 percent sulfur 1000nm pitch design

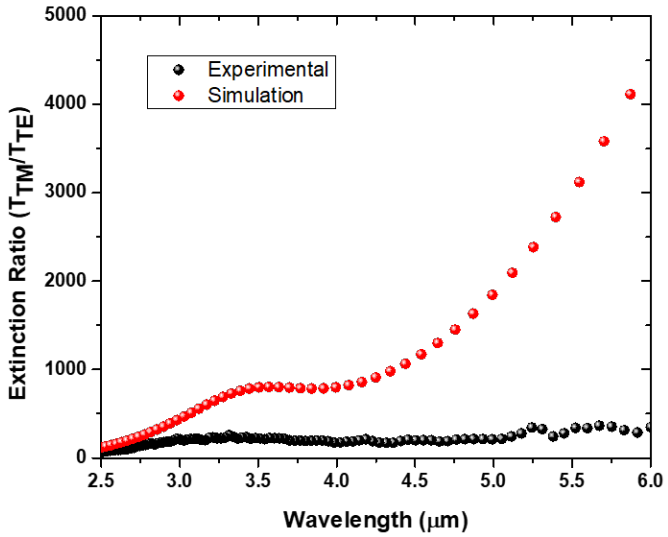

Figure 5.5. Extinction ratio simulation and experiment results overlay of 35 percent sulfur 1000nm pitch design

Fig. 5.2 shows a simulation of the ideal structure of the wire grid sample for both the TM transmission and TE transmission. Fig. 5.5 shows the extinction ratio for the 1000nm wire grid sample. Fig. 5.4 shows the simulation data overlaid with the experimental data for the 1000 nm pitch grating sample TM transmission and TE transmission. The experimental sample has nearly identical TM transmission in MIR when compared to the simulation of the ideal design structure. The high level of agreement shows that the sample structure dimensions were successfully replicated and that the sulfur polymer material was well characterized. The increase in TM transmission just past 3.5 μm is achieve by Fabry–Pérot internal resonance and can shift location based on the sulfur film thickness, t_{sf}, as seen in Fig. 5.6.

With the experimental and simulation TM transmission both having the same peak location (3.5 μm) the t_{sf} is shown to match the design thickness of 1000nm. Fig. 5.5 shows the simulation data overlaid with the experimental data for the 1000 nm pitch grating sample extinction ratio. Initially the experimental extinction ratio is at the same level as the simulation, but as the wavelength increases over 2.75 μm

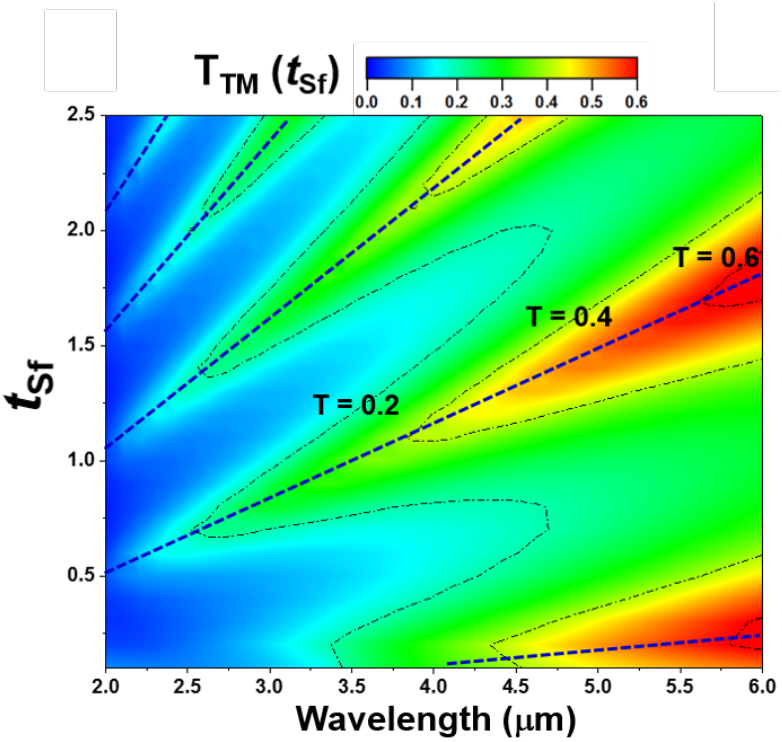

Figure 5.6. Simulation result of TM transmission as the wavelength (x axis) and sulfur polymer film thickness (y axis) vary

the simulation extinction ratio became increasingly greater than the experimental. The gap in extinction ratio performance is due to the difference in TE transmission between the experimental and simulation data. The low TE transmission in the experimental data is partly due to defects in sample fabrication, such as Au on the side walls, and partly due to the resolution limitations of FTIR TE transmission measurements beyond 10^{-3}.

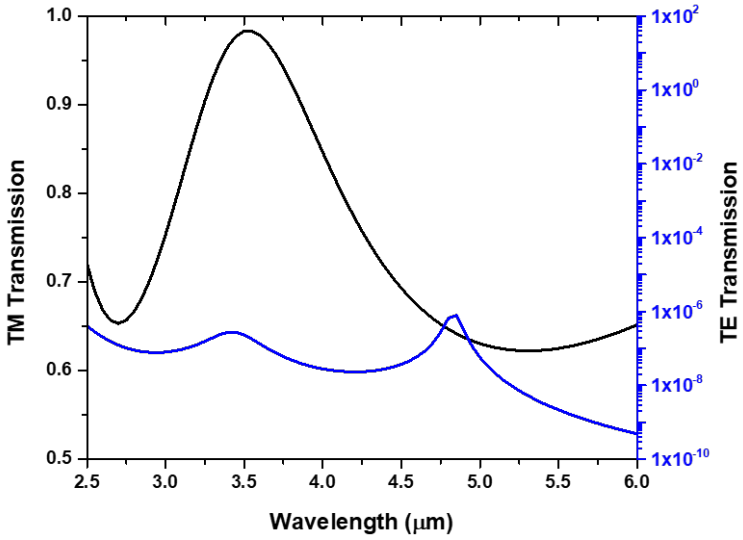

Figure 5.7. TM and TE transmission simulation of 35 percent sulfur 700nm pitch design

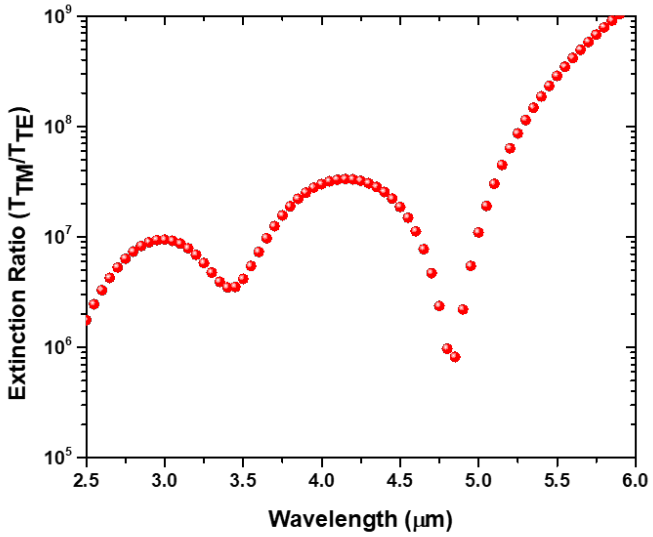

Figure 5.8. Extinction ratio simulation of 35 percent sulfur 700nm pitch design

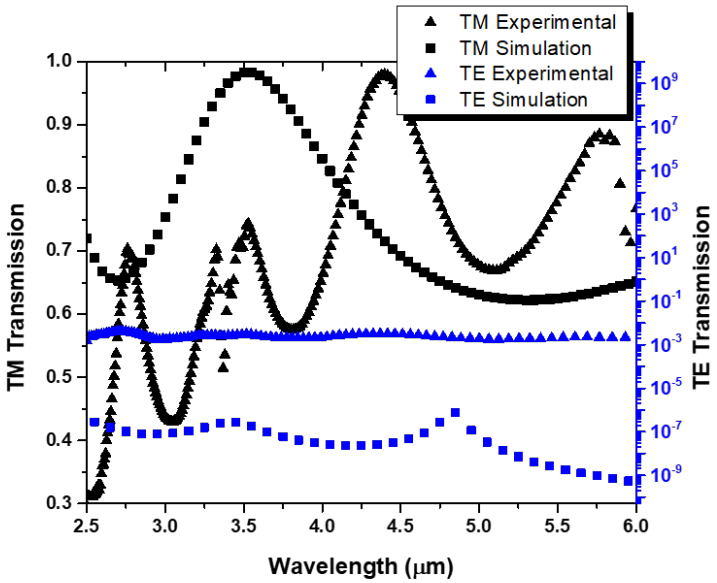

Figure 5.9. TM and TE transmission simulation and experiment results overlay of 35 percent sulfur 700nm pitch design

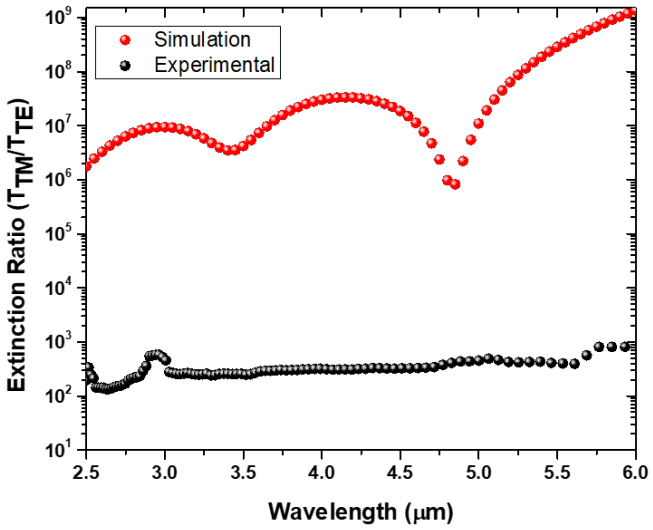

Figure 5.10. Extinction ratio simulation and experiment results overlay of 35 percent sulfur 700nm pitch design

Fig. 5.7 shows the simulation of the ideal structure for the wire grid sample for both the TM transmission and TE transmission. Fig. 5.10 shows the extinction ratio for the 700nm wire grid sample. Fig. 5.9 shows the simulation data overlaid with the experimental data for the 700 nm pitch grating sample TM transmission and TE transmission. Fig. 5.5 shows the simulation data overlaid with the experimental data for the 1000 nm pitch grating sample extinction ratio. There is a clear discrepancy in the location of the peaks and the transmission levels between the simulation data and the experimental data.

To understand the discrepancy between the simulation and experimental data, the simulation grating dimensions were compared to the actual dimensions of the sample. For accurate dimensions of the 700nm pitch sample cross section SEM analysis was required; Fig. 5.11 shows the 700nm sample cross section. It can clearly be seen that the sulfur film thickness ,t_{sf}, was more than four times thicker than what the original design thickness of 1 μm. Also as pointed out earlier, there were some fabrication imperfections of rounded corners on the gratings. The COMSOL simulation was adjusted to reflect the measured experimental sample dimensions. The results of the new simulation are shown on Fig. 5.12 shows the 700nm pitch simulation with the thickened sulfur film as well as the fabrication imperfections of the rounded corners.

With the modification in the simulation design the cause of the peak location discrepancy in TM transmission is now clear. With a larger layer of sulfur polymer above the Si wafer the light had a much larger area to reflect and interfere creating multiple peaks and troughs in the TM transmission. By solving for the TM transmission over both sulfur film thickness and wavelength, Fig. 5.13 shows the color map of the different resonance peaks in TM transmission as the wavelength and sulfur polymer film thickness change.

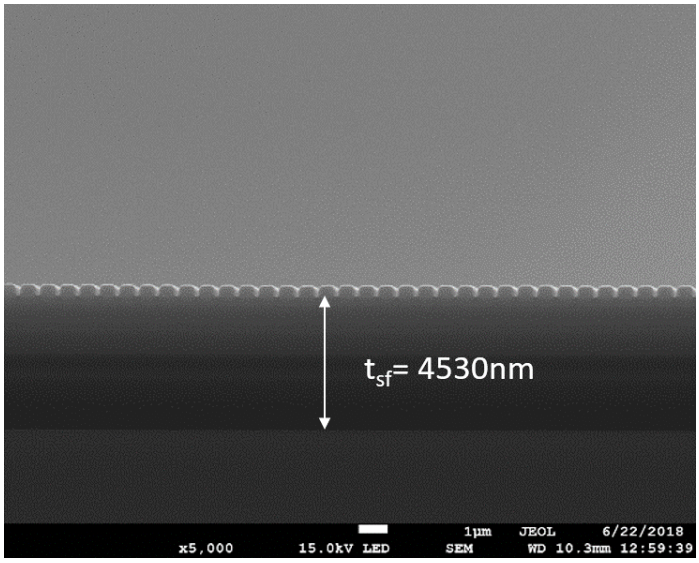

Figure 5.11. Cross section SEM of 700nm pitch sample showing the t_{sf} of 4530nm compared to design dimension of 1000nm

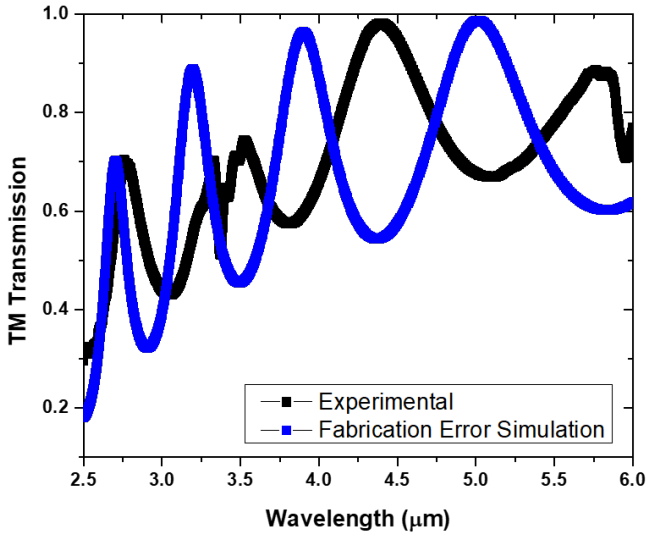

Figure 5.12. TM transmission simulation and experiment results overlay of 35 percent sulfur 700nm pitch design after simulation modification

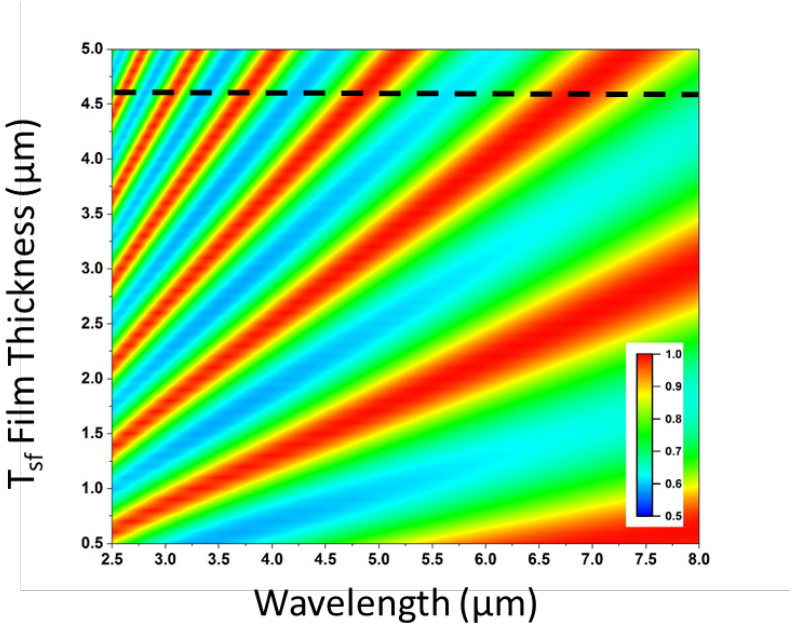

Figure 5.13. Simulation result of TM transmission as the wavelength (x axis) and sulfur polymer film thickness (y axis) vary. Dotted line represents the film thickness of the fabricated sample

When the film thickness is 4.6 μm there are peaks seen at 2.5μm, 3.0μm, 3.5μm, 4.75μm, and 6.75 μm in the TM transmission. Similar results can be seen in the experimental results overlaid in Fig. 5.12 where the TM transmission shows corresponding peaks at the same wavelength locations. With TM transmission at almost 100 percent and TE at almost zero, the performance of the 700 nm pitch sample is exceptional and with the additional simulation, the increase in TM transmission peaks is explained.

6. SUMMARY, CONCLUSION AND RECOMMENDATIONS

6.1 Summary and Conclusion

Herein, a novel polymer was fabricated and characterized, original 1-D subwavelength grating structures were designed and fabricated, wire grid polarizer were fabricated, tested, and simulated to enhance performance in MIR polymer polarizers.

Sulfur polymer was successfully synthesized and used to form viable 1D grating samples. The sulfur polymer was shown with ellipsometry to be ideal for use in high index polymer applications, with a refractive index over 1.6 for 35 percent sulfur based polymer.

1D grating polarizer molds were designed based of the properties of electromagnetic wave interaction with repeating subwavelength grid patterns, surface plasmonics, and FabryProt resonance. The grating designs were modeled, and the molds were fabricated at Argonne National Lab to then be used as the mold for the stamps.

High quality wire grid polarizer samples were fabricated using the master molds, nanoimprinting, and a thermal curing method. These samples were then tested with FTIR to measure their performance as polarizers by comparing the TM and TE transmission data.

Simulation validated the design and shows how different changes in the design can affect the performance of the samples. The 35 percent sulfur 1000 nm pitch sample had TM transmission of 32 percent and an extinction ratio of 375. The 35 percent sulfur 700 nm pitch sample had TM transmission of 98 percent and an extinction ratio of 600.

In conclusion, both samples were highly successful and produced accurate results that were reflected in the simulation data. The feasibility of using sulfur polymer as the structural and dielectric material in MIR polarizers is proven to be successful and opens the door to further research with this material. Proving that a polymer based

material can form a high functioning surface mountable polarizer also increases the applications of nanoimprinting in the field of optics and polarimetric imaging.

6.2 Recommendations

1. Recommendations for future work include examining the combination of different grating designs with varying pitch as well as varying the sulfur polymer film thickness to shift the peak transmission peak across the MIR wavelength.

2. Fabrication of grating samples with sulfur polymer in different weight percentages of sulfur. By varying the sulfur polymer to DIB ratio the polymer can have a varying refractive index and can be used to tune the optical performance of the material and also used to create gradient index materials.

3. Another topic of interest would be the combination of sulfur polymer with other binding agents and nanoparticles to create a more stable and higher index composite materials that do not rely on DIB for polymer stabilization. Some examples of these agents include ZnS and ZnSe nanoparticle composites formed with molten sulfur.

REFERENCES

REFERENCES

[1] Lisa Hutchinson. Imaging: Digital infrared breast scan shows promise for detecting cancer. *Nat Rev Clin Oncol*, 7(9):483–483, 2010.

[2] A. Rogalski, J. Antoszewski, and L. Faraone. Third-generation infrared photodetector arrays. *Journal of Applied Physics*, 105(9):091101, 2009.

[3] J. Scott Tyo, Dennis L. Goldstein, David B. Chenault, and Joseph A. Shaw. Review of passive imaging polarimetry for remote sensing applications. *Applied Optics*, 45(22):5453–5469, 2006.

[4] Mukul Sarkar, David San Segundo Bello, Chris van Hoof, and Albert J. P. Theuwissen. Biologically inspired cmos image sensor for fast motion and polarization detection. *IEEE Sensors Journal*, 13(3):1065–1073, 2013.

[5] A. G. Andreou and Z. K. Kalayjian. Polarization imaging: Principles and integrated polarimeters. *IEEE Sensors Journal*, 2(6):566–576, 2002.

[6] Henry A Francis. Method of forming fine wire grids, December 13 1966. US Patent 3,291,871.

[7] Xing-Jie Yu and Hoi-Sing Kwok. Application of wire-grid polarizers to projection displays. *Appl. Opt.*, 42(31):6335–6341, Nov 2003.

[8] S.-W. Ahn, K.-D. Lee, J.-S. Kim, S. H. Kim, J.-D. Park, S.-H. Lee, and P.-W. Yoon. Fabrication of a 50 nm half-pitch wire grid polarizer using nanoimprint lithography. *Nanotechnology*, 16:1874–1877, September 2005.

[9] Yasin Ekinci, Harun H. Solak, Christian David, and Hans Sigg. Bilayer al wire-grids as broadband and high-performance polarizers. *Opt. Express*, 14(6):2323–2334, Mar 2006.

[10] XJ Yu and Hoi Sing Kwok. Optical wire-grid polarizers at oblique angles of incidence. *Journal of applied physics*, 93(8):4407–4412, 2003.

[11] Seh-Won Ahn, Ki-Dong Lee, Jin-Sung Kim, Sang Hoon Kim, Joo-Do Park, Sarng-Hoon Lee, and Phil-Won Yoon. Fabrication of a 50 nm half-pitch wire grid polarizer using nanoimprint lithography. *Nanotechnology*, 16(9):1874, 2005.

[12] Itsunari Yamada, Kenji Kintaka, Junji Nishii, Satoshi Akioka, Yutaka Yamagishi, and Mitsunori Saito. Mid-infrared wire-grid polarizer with silicides. *Optics letters*, 33(3):258–260, 2008.

[13] Kristan P Gurton, Alex J Yuffa, and Gorden W Videen. Enhanced facial recognition for thermal imagery using polarimetric imaging. *Optics letters*, 39(13):3857–3859, 2014.

[14] Thomas Weber, Thomas Ksebier, Ernst-Bernhard Kley, and Andreas Tnnermann. Broadband iridium wire grid polarizer for uv applications. *Optics letters*, 36(4):445–447, 2011.

[15] Yasin Ekinci, Harun H Solak, Christian David, and Hans Sigg. Bilayer al wire-grids as broadband and high-performance polarizers. *Optics express*, 14(6):2323–2334, 2006.

[16] J. J. Griebel, S. Namnabat, E. T. Kim, R. Himmelhuber, D. H. Moronta, W. J. Chung, A. G. Simmonds, K. J. Kim, J. van der Laan, N. A. Nguyen, E. L. Dereniak, M. E. Mackay, K. Char, R. S. Glass, R. A. Norwood, and J. Pyun. New infrared transmitting material via inverse vulcanization of elemental sulfur to prepare high refractive index polymers. *Adv Mater*, 26(19):3014–8, 2014.

[17] X.H. Zhang, Y. Guimond, and Y. Bellec. Production of complex chalcogenide glass optics by molding for thermal imaging. *Journal of Non-Crystalline Solids*, 326, 327:519–523, 2003.

[18] M. Aven, D. T. F. Marple, and B. Segall. Electrical and optical properties of znse. *Journal of Applied Physics*, 32(10):2261–2265, 1961.

[19] Seh-Won Ahn, Ki-Dong Lee, Jin-Sung Kim, Sang Hoon Kim, Joo-Do Park, Sarng-Hoon Lee, and Phil-Won Yoon. Fabrication of a 50 nm half-pitch wire grid polarizer using nanoimprint lithography. *Nanotechnology*, 16(9):1874, 2005.

[20] Ming Ma, David S Meyaard, Qifeng Shan, Jaehee Cho, E Fred Schubert, Gi Bum Kim, Min-Ho Kim, and Cheolsoo Sone. Polarized light emission from gainn light-emitting diodes embedded with subwavelength aluminum wire-grid polarizers. *Applied Physics Letters*, 101(6):061103, 2012.

[21] Liang Zhang, Jing Hua Teng, Soo Jin Chua, and Eugene A Fitzgerald. Linearly polarized light emission from ingan light emitting diode with subwavelength metallic nanograting. *Applied Physics Letters*, 95(26):261110, 2009.

[22] Zhaoning Yu, Paru Deshpande, Wei Wu, Jian Wang, and Stephen Y Chou. Reflective polarizer based on a stacked double-layer subwavelength metal grating structure fabricated using nanoimprint lithography. *Applied Physics Letters*, 77(7):927–929, 2000.

[23] C Genet and TW Ebbesen. Light in tiny holes. In *Nanoscience And Technology: A Collection of Reviews from Nature Journals*, pages 205–212. World Scientific, 2010.

[24] Rei Kitamura, Laurent Pilon, and Miroslaw Jonasz. Optical constants of silica glass from extreme ultraviolet to far infrared at near room temperature. *Applied Optics*, 46(33):8118–8133, 2007.

[25] Zhaoning Yu, Paru Deshpande, Wei Wu, Jian Wang, and Stephen Y Chou. Reflective polarizer based on a stacked double-layer subwavelength metal grating structure fabricated using nanoimprint lithography. *Applied Physics Letters*, 77(7):927–929, 2000.

[26] Sang Hyun Je, Onur Buyukcakir, Daeok Kim, and Ali Coskun. Direct utilization of elemental sulfur in the synthesis of microporous polymers for natural gas sweetening. *Chem*, 1(3):482–493, 2016.

[27] Woo Jin Chung, Jared J Griebel, Eui Tae Kim, Hyunsik Yoon, Adam G Simmonds, Hyun Jun Ji, Philip T Dirlam, Richard S Glass, Jeong Jae Wie, Ngoc A Nguyen, et al. The use of elemental sulfur as an alternative feedstock for polymeric materials. *Nature chemistry*, 5(6):518, 2013.

[28] R Walraven. Polarization imagery. *Optical Engineering*, 20(1):200114, 1981.

[29] Kristan P Gurton and Melvin Felton. Remote detection of buried land-mines and ieds using lwir polarimetric imaging. *Optics express*, 20(20):22344–22359, 2012.

[30] Libing Zhou and Wen Liu. Broadband polarizing beam splitter with an embedded metal-wire nanograting. *Optics letters*, 30(12):1434–1436, 2005.

[31] Libing Zhou, Wen Liu, Qing Liu, Liang Zhang, and Tao Yang. A novel nano-optics polarization beam splitter/combiner for telecom applications. In *Passive Components and Fiber-based Devices*, volume 5623, pages 248–254. International Society for Optics and Photonics.

[32] Ting Xu, Yi-Kuei Wu, Xiangang Luo, and L Jay Guo. Plasmonic nanoresonators for high-resolution colour filtering and spectral imaging. *Nature communications*, 1:59, 2010.

[33] Anni Lehmuskero, Markku Kuittinen, and Pasi Vahimaa. Refractive index and extinction coefficient dependence of thin al and ir films on deposition technique and thickness. *Optics express*, 15(17):10744–10752, 2007.

[34] A Yamaguchi, RB Penland, S Mizushima, TJ Lane, Columba Curran, and JV Quagliano. Infrared absorption spectra of inorganic coördination complexes. xiv. infrared studies of some metal thiourea complexes1a. *Journal of the American Chemical Society*, 80(3):527–529, 1958.

[35] Donald L Pavia, Gary M Lampman, George S Kriz, and James A Vyvyan. *Introduction to spectroscopy*. Cengage Learning, 2008.

[36] S Tibuleac and R Magnusson. Reflection and transmission guided-mode resonance filters. *JOSA A*, 14(7):1617–1626, 1997.

[37] MG Moharam, Drew A Pommet, Eric B Grann, and TK Gaylord. Stable implementation of the rigorous coupled-wave analysis for surface-relief gratings: enhanced transmittance matrix approach. *JOSA A*, 12(5):1077–1086, 1995.